Chemical Erosion of DIII-D Tokamak Tile Samples

Patrick B. Wright

A thesis submitted in conformity
with the requirements for the degree of
Master of Applied Science
University of Toronto [1]

January 30, 2001

Chemical Erosion of DIII-D Tokamak Tile Samples

Master of Applied Science 2001
Patrick B. Wright
Institute for Aerospace Studies
University of Toronto

Abstract

Pieces of divertor and midplane tiles from DIII-D have been studied to determine their erosion characteristics under low-energy deuterium impact (50 eV and 200 eV) as a function of fluence for sample temperatures of 300 K, 500 K, and 700 K. At the outer midplane, laboratory measurements of erosion yields were initially found to be consistent with boron-doped graphite. The erosion yields decreased by a factor of 1.5 – 2 with increasing D^+ fluence in the range of $4 \times 10^{21} - 3 \times 10^{22}$ D^+/m^2, and levelled off for fluences $\geq 3 \times 10^{22}$ D^+/m^2. Chemical erosion yields of the inner divertor sample were found to be comparable to that of pure graphite for incident D^+ energies of 50 eV and sample temperatures of 300 K and 500 K. Visual inspection indicated that the film was eroded through to the graphite substrate, confirming the observed chemical erosion results.

Acknowledgements

I would like to thank Dr. Anthony A. Haasz for his continued support throughout this project. I would also like to thank Dr. Jim W. Davis, whose guidance, encouragement, and patience have made this thesis possible. And, of course, I need to thank Pete Schwanke, Mike Poon, Rick Macaulay-Newcomb, David Elder, Allen Chen, Cliff Hamilton, Charles Perez, and Ian Youle for their valuable contributions and comaraderie all those long days and late nights in the lab.

Contents

List of Figures

1 Introduction and Background

1.1 Fusion Energy

At the beginning of a new millenium, it is becoming increasingly clear that the world is in need of an abundant, safe, environmentally acceptable, and cost-competitive source of energy. Future global energy demand will depend on rates of growth of population and economic activity, as well as reduction of energy usage, i.e., energy conservation. Although studies vary, many long-term projections of world energy demand predict consumption levels 2 - 3 times their current levels by the year 2050 [1]; this is commonly attributed to the pursuit of rapid economic development in less developed nations, combined with high population growth rates. Of the total primary energy used in the world in 1985, nearly 30% was used in the generation of electricity, while 70% was used for heat, motive power, and other non-electrical applications [1]. In both cases, the burning of fossil fuels (oil, gas, and coal) was the main contributor. Coal, oil, and gas all release carbon dioxide and other gases into the atmosphere, creating adverse effects on the earth's climate, including the risk of global warming and acid rain. These effects are perceived with increasing concern, both in public opinion and at the governmental level.

Whatever the quantity of energy which will be required, it must be produced in an economically and environmentally acceptable manner. Nuclear fusion as a commercial source of energy has many attractive attributes:

- The fuel supply is extractable from ordinary seawater and is sufficient in quantity for millions of years;
- Nuclear fusion produces no greenhouse gas emissions;
- There are advantages over many forms of renewable energy (i.e., hydro, solar, wind) with respect to impacts on ecological and geophysical processes;
- Fusion does not carry the same risk of radiological hazard as fission energy;
- The monetary costs of fusion are expected to be comparable to those of other medium and long-term options.

It is interesting to note that in the United States, there has been a remarkably strong correlation between fusion research funding and crude oil prices [2]. For example, 25 years ago the fusion research program was accelerated as oil prices soared in response to an OPEC-driven supply crisis. Even despite substanstial successes in fusion research since the seventies, including pushing temperature, density, and confinement parameters to reactor grade levels, funding for fusion research has mirrored supply and demand circumstances for oil. The seventies saw ambitious plans for the development of fusion energy, but budgets limited their implementation. Cold war politics in the eighties have led to the proposed International Thermonuclear Experimental Reactor (ITER) as a centerpiece of international

collaboration and the next step in fusion energy. With the end of the cold war, political support for ITER has diminished. Today, the fusion program is confronted by cheap oil prices and the perception that fusion electricity will be too expensive: over the past decade, funding has replaced time as the primary constraint for the development of fusion energy [2].

1.2 Nuclear Fusion

In 1905, Albert Einstein postulated that mass can be conveted into energy, according to his famous formula $E = mc^2$, and it was not long before speculations were made as to how to tap this potential source. Of the several candidate fusion reactions, deuterium-tritium fusion is the most easily achieved, and therefore is most likely to be used in the first fusion reactor. The D-T reaction proceeds as:

$$D + T \implies {}^4He + n + 17.6MeV$$

In order to achieve fusion, ions must have sufficient energy to overcome the Coulomb repulsion between the two nuclei. By heating the atoms to very high temperatures ($> 100 \times 10^6$K), the tail of the Maxwellian velocity distribution (along with quantum tunneling effects) allows enough ions to fuse. Today, one of the most promising schemes for the realization of controlled nuclear fusion is the tokamak concept.

When gaseous deuterium and tritium are heated to the temperatures required for fusion, they become a seething mass of ions and electrons called a plasma. Unless these particles are confined in some manner, they will escape the plasma in microseconds. Because plasma particles are fully ionized, they are susceptible to the influence of a magnetic field. Charged particles are free to move along magnetic field lines, but will orbit the field lines according to the Lorentz force, with a cyclotron frequency of $\omega_c = eB/m$, thus carrying out a helical motion. The tokamak concept (figure 1) employs a toroidal reactor vessel with magnetic field coils surrounding the vessel providing a $\vec{B}$-field in the toroidal direction. Surrounding this structure is a set of transformer coils which uses the plasma as its secondary winding to create an axial current, and hence a poloidal magnetic field. The net magnetic field of this arrangement is helical around the torus which provides excellent confinement of the plasma and its energy.

1.3 Plasma Surface Interactions

Unfortunately, the plasma confinement of the tokamak scheme is not perfect. Plasma particles can escape from the core plasma by self diffusion due to Coulombic collisions and by anomolous transport through microinstabilities. Outside the last closed flux surface is a region called the scrape off layer (SOL), where the magnetic field lines end on the vessel wall. A more complete treatment of the SOL and its properties can be found in [3].

When plasma particles are incident on the inner walls of a reactor vessel, they can either be reflected or penetrate the surface. These impacting particles will typically erode

the plasma-facing material, which in turn can enter the SOL and be transported back into the main plasma where it not only dilutes the fusion fuel, but also cools the core through brehmsstralung radiation. The tolerance of the plasma to impurities is an important constraint to ignition, and depends on the atomic weight, Z, of the eroded material.

Furthermore, during operation, materials at different locations of the reactor will be subjected to significantly different conditions. The main wall will experience fluxes of charge exchange neutrals with energies ranging from a few eV to keV's, while divertor targets and sidewalls see much higher fluxes of hydrogen with 10's of eV. Three main erosion mechanisms can be defined for the interaction between plasma particles and the plasma-facing components:

Physical Sputtering: Substrate particles are emitted due to a direct transfer of momentum from the incident particle to the target matrix atom. This effect requires that incident particles have energies greater than a particluar threshold energy characteristic of the target-projectile combination.

Radiation-Enhanced Sublimation (RES): This erosion mechanism is unique to carbon-based materials. RES is induced by energetic particle impact above a certain threshold energy at temperatures greater than 1200K. Interstitial-vacancy pairs are formed in the implantation zone, and at sufficiently high temperature will diffuse to the surface and are released with thermal enegies of a few eV.

Chemical Erosion: Occurs when chemically reactive plasma species come into contact with plasma-facing materials, releasing molecular reaction products from the surface. This process occurs at all energies, and there is no evidence of a threshold.

There are still many aspects of plasma surface-interactions that are not adequately understood. Control of these processes is vital for control of both SOL and core plasma parameters.

1.4 Chemical Erosion of Carbon

Due to its low atomic number and excellent thermo-mechanical properties, carbon in the form of graphite is a primary candidate as a plasma-facing material. Since deuterium and tritium will be the fuel in future reactors, these plasma species will dominate the flux of particles to the plasma-facing materials. These ion species will have bombarding energies of $\sim 2kT_i + 3kT_e$ [4], which corresponds to energies of 10's to 100's of eV depending on the edge plasma temperature. Furthermore, first wall components are also subjected to charge exchange neutrals with energies ranging from 10 eV to keV's and Frank-Condon atoms with a few eV, as well as energetic impurity and helium ash ions, neutrons and electrons. All of these influence the chemical erosion of carbon materials; in fact, the combination of all of these particle sources can lead to synergistic effects in erosion yields. Further complicating

the erosion of graphite is the wide range of particle fluxes expected in tokamak devices, ranging from $\sim 10^{18} D/m^2 s$ of energetic neutrals, $\sim 10^{20} - 10^{22} D^+/m^2 s$ on the vessel walls, to $\sim 10^{23} D^+/m^2 s$ at the divertor plates. The jury is still out as to the flux dependence of chemical erosion. A brief review of results relevant to this thesis is presented here.

Chemical Erosion in Tokamaks

The importance of chemical erosion with respect to impurity production in tokamaks, in particular the relative role of hydrocarbon formation compared to physical sputtering of carbon atoms, is still a matter of contention in the fusion community [4, 5]. However, the use of optical emission spectroscopy (OES) has conclusively demonstrated the presence of hydrocarbon formation in tokamaks. CD line emissions have been observed in ASDEX [6, 7], JET [7], DITE [8], TEXTOR [9], TORE SUPRA [10], and DIII-D [35] for deuterium discharges. Maximum methane yields (at T_m) were derived, under certain assumptions of plasma parameters and photon efficiency, from the emission spectra in ASDEX, DIII-D, JET, TEXTOR, and TORA SUPRA, and fell in the range 0.01-0.05 CD_4/D. These results are in agreement with the TEXTOR sniffer probe experiments [11, 12] where hydrocarbon formation yields were measured using the SOL as a high flux density ion source.

Despite these results, the effect of chemical erosion on tokamak core plasma impurity levels is still uncertain. Reasons for this uncertainty include:

- unpredictability of wall component surface temperatures; chemical erosion yields are strongly temperature dependent, varying by as much as an order of magnitude;
- assuming a finite reaction time, the reaction will saturate at sufficiently high flux densities, although this saturation level is still under debate;
- in multi-element wall materials (as is presently the case for ITER), multi-species bombardment on graphitic materials may result in synergisms or alter the erosion mechanisms.

The fact that the total carbon found at the divertor strike points can be accounted for by physical sputtering alone suggests that there is a prompt redeposition of the hydrocarbon products and dissociation fragments, or that there is a strong flux dependence on the chemical erosion yield [5]. However, away from the strike points, physical sputtering alone is not enough to account for the impurity carbon levels. Discharges with helium plasmas show that the discrepancy is most likely due to chemical sputtering [5]. The source of the chemical erosion is still not clear [13].

Chemical Erosion in the Laboratory

The mechanisms leading to the observed chemical erosion phenomena in tokamaks are very difficult to identify due to the complexity of the plasma-surface interaction processes. Therefore, a good understanding of the controlling processes involved in these mechanisms

is necessary in order to select suitable materials for plasma-facing components. In order to isolate these processes and their underlying mechanisms, controlled laboratory experiments are being conducted. A number of reviews of available results can be found in [5, 13, 14]. More recent weight loss measurements of chemical erosion of graphite can be found in [15]. The ensuing discussion will be limited to results which are pertinent to this thesis.

Data accumulated from various investigations of hydrocarbon formation due to the bombardment of carbon by energetic hydrogen ions is in fair agreement. Figure 2 shows the chemical erosion yield of methane as a function of temperature for incident hydrogen and deuterium bombardment for energies of 50 eV - 1000 eV. These plots show that the erosion yields reach a maximum for temperatures of ~750–800 K, with peak yields of $\sim 0.15 CD_4/D$ at 1000 eV and $\sim 0.02-0.04 CD_4/D$ at 50 eV [16, 17, 18]. Furthermore, as the ion energy is decreased, a broadening of the temperature profile is observed, accompanied by a reduction in the maximum erosion yield and a shift in the temperature of the peak yield, T_m, to lower temperatures. As seen in figure 3 [5, 20], this trend is seen to continue for energies $\leq$50 eV. It is also seen (figure 4) that there is an increasing contribution from the C_2 and C_3 groups to the total carbon erosion yield with decreasing impact energy [20]. For impact energies of ~3 keV, there is about a 10% contribution from the heavier hydrocarbons [21], increasing to roughly 50% at 50 eV [20], and continuing down to sub-eV H^0 impact where the contribution to total carbon erosion from heavier hydrocarbons in about an order of magnitude higher than the contribution from methane [20].

From these obsevations, it has been proposed that there exists two reaction mechanisms that contribute to the formation of methane in graphite subjected to D^+ irradiation [13]. One mechanism dominates at higher temperatures and energies greater than ~100 eV, and leads to the formation of CD_3 radicals with a maximum yield occuring at ~800 K. The second mechanism, which becomes important at lower temperatures and lower ion energies, gives rise to the formation of CD_4 molecules, and may have a maximum yield for temperatures as low as 200 K [19].

1.5 Effect of Boron Dopants in Carbon

Various attempts to reduce the chemical erosion of graphite have been made, leading to the introduction of dopants into the carbon matrix or onto the surfaces of plasma-facing materials in fusion devices. Characterization and chemical erosion experiments on amorphous hydrogenated boron-carbon films have been conducted [22, 23, 24] with varied results as to the suppression of hydrocarbon formation. Boron doping of graphite, on the other hand, has been found to drastically alter the erosion characteristics of the carbon. For example, chemical erosion of B_4C due to 1 keV H^+ ions was found to be very small [25]. The overall reduction, however, is seen to be greatest for temperatures $\geq T_m$ [25, 26, 27, 28]. Figure 5 shows the erosion yield temperature profiles for pyrolytic graphite and USB15 (15% boron doped graphite) for various D^+ impact energies [26]. For sample temperatures less than ~600 K there is no appreciable difference in the yields of the two materials. Similar results were found in chemical erosion experiments with TiB_2-doped graphite [28], where

erosion yields were found to decrease by a factor of 4–10 as compared with pure graphite for energies ≥300 eV and temperatures ≥700 K. At lower temperatures and energies (~30 eV), the erosion yield was comparable to that of graphite, accounting for the reduction in carbon content due to doping, implying that the dopants do not play a role in the erosion mechanism at low temperature and energy, other than to physically cover the carbon.

These results support the hypothesis [13] that two reaction channels exist for the chemical erosion of carbon based materials. The boron doping of the graphite appears to suppress the high temperature mechanism, while leaving the low temperature channel unchanged [13]. This suppression of the high temperature channel leads to the characteristic shift of T_m to lower temperatures in boron-doped graphites [13]. It is important to note, however, that at lower temperatures and energies (expected conditions in next generation fusion devices) the dopants do not cause a significant reduction in the chemical erosion yield.

Boronization

In addition to the doping of graphitic materials, attempts to reduce chemical erosion have been made by depositing thin films onto the plasma-facing carbon components. This has led to a process called boronization, which is the plasma chemical vapour deposition of a thin a-B/C:H film on the first wall of fusion devices. As a result of boronization, a significant reduction in core plasma impurities has been observed, including carbon, oxygen, and heavier elements (i.e., iron, nickel and chromium) leading to an improvement in tokamak discharges [29, 31]. The improvement in plasma performance is primarily due to oxygen gettering effects, as well as the suppression of chemical erosion of carbon materials [13]. The boronization process was pioneered in TEXTOR [31], and has been performed in most tokamak fusion devices, including ASDEX [30], TORA SUPRA [32], TFTR [33], and DIII-D [34]. Since this thesis is concerned with the chemical erosion of DIII-D tile samples, some discussion of the DIII-D tokamak is warranted, and will be presented here.

1.6 The DIII-D Tokamak

With the ultimate goal of creating a safe, steady-state source of energy employing fusion principles, numerous research centres and test facilities have been developed around the world. One of these facilities was the Doublet III tokamak, which was built in the late 1970's by General Atomics. The primary purpose of Doublet III was to be a flexible facility investigating the advantages of non-circular plasma cross-sections. A new, larger D-shaped vacuum vessel replaced the old doublet shaped vessel after seven years of operation as Doublet III, and the tokamak became known as DIII-D. The coil systems were adjusted to fit the new vessel, an extra generator was added, and the neutral beams were upgraded enabling longer pulse duration, greater power, and better reliability. The new DIII-D facility is capable of a wide range of plasma operating conditions, and the recent addition of a new divertor has significantly improved plasma confinement and stability. In addition, in the fall of 1992 DIII-D switched all plasma-facing surfaces to 100% carbon coverage, from ~40%

previously [35]. Previously installed graphite tiles were cleaned by baking and grit-blasting, and re-installed. Starting with the 1993 operational period, the DIII-D wall was considered to be 100% virgin graphite [35].

Boronization in DIII-D

Boronization was performed in the DIII-D tokamak using a pulsed glow discharge (to provide toroidal homogeneity) and a mixture of helium (90%) and deuterated diborane, B_2D_6, (10%) gases [34]. The gas mixture was spread out along the vessel wall at low current (0.5 A) for ~2 seconds, and then deposited more intensely for 1 second during a high current (5 A) pulse. As a result, carbon, oxygen and nickel impurities were substantially reduced, lowering the core plasma Z_{eff}, and hence the radiated power, although oxygen remained the primary radiation source. This led to an improved plasma confinement called VH mode, observed for the first time in DIII-D. This new confinement mode is characterized by a confinement time 1.5–2 times higher than that predicted by H-mode scaling [34]. The boron film was sufficient to achieve VH-mode discharges during 150 post-boronization shots. It has also been seen that the erosion characteristics of the DIII-D divertor surfaces have evolved with increasing number of boronizations [35]. This effect is examined below.

A comprehensive spectroscopic study of carbon sources and core plasma carbon impurity content has been performed in the DIII-D tokamak since the installation of graphite tiles on plasma-facing surfaces in the fall of 1992 [35]. In-situ atomic, molecular, and charge exchange recombination spectroscopy has observed that the chemical erosion rate in the lower divertor has evolved over the last eight years of operation, with the average Y_{chem} having decreased by a factor of ~10 since the installation of the virgin graphite tiles. Since 1993, DIII-D plasma-facing surfaces have experienced $\sim 10^5$ seconds of plasma exposure, and ~30 boronizations of 100–150 nm each, resulting in a cumulative boron layer of 3–5 μm. Figure 6 shows that the $B_{CD}/B_{D\gamma}$ ratio (B_{CD} being an indicator of chemical erosion) in the lower divertor region has decreased by a factor of 10–20 in the past eight years. A direct comparison of the $B_{CD}/B_{D\gamma}$ ratio for two nearly identical shots from 1993 and 1999 is shown in figure 7, and demonstrates the reduction in chemical erosion across the lower divertor [35]. The reduction in erosion at the lower divertor was thought to be due to boronization (or perhaps some other form of plasma conditioning process) of the inner vessel wall. However, surfaces in the vicinity of the divertor strike points are prone to large net erosion or net deposition rates, and hence deposited boron would be quickly removed, or covered by a thick deposit.

Despite this reduction in the carbon source from the lower divertor, the core carbon content has remained roughly constant (see figure 8). There is a fair amount of scatter in the data, but on average a core carbon impurity content of 2–3% is seen for the H-mode discharges. It is also found that there has been no significant decrease in the chemical erosion yield at the outer midplane. Estimates of chemical erosion, based on measurements made by a survey (100-1000Å) vacuum ultra-violet (SPRED) spectrometer, are comparable to that of pure graphite and do not change with time. These can be found in figure 9 [35]. In the region of the outer midplane, the ion flux is not considered to be sufficient to remove

the deposited boron, and consequently should not be a significant source of carbon. In light of these contradictory measurements, it was resolved to perform controlled laboratory experiments in an attempt to glean some insight into the observed tokamak results.

1.7 Thesis Objective

Tile samples from the divertor and outer midplane regions (see figure 10) have been obtained. The objective of this thesis is to perform low-energy ion-beam experiments in a controlled laboratory environment at the University of Toronto in order to determine the chemical erosion yields of the boronized samples, with the aim of shedding some light on the contradictory measurements made in DIII-D. This will be pursued by performing experimental measurements of the chemical erosion yields of DIII-D boronized graphite divertor and midplane tile samples (including methane, heavy hydrocarbons, and boron containing molecules) as a function of incident ion fluence under low energy deuterium impact at energies of 50 eV and 200 eV, and for temperatures of 300 K, 500 K, and 700 K (roughly mirroring DIII-D operating conditions). Surface analysis will also be performed on all samples in order to synthesize a more complete picture of the processes involved. In the following sections, details of the experimental procedure and the experimental results are presented.

2 The Experiment

All chemical erosion experiments outlined in this thesis were conducted in an ultrahigh vacuum (UHV) system in the Fusion Materials Research Lab of the University of Toronto Institute for Aerospace Studies. This section outlines the experimental facility and its operational characteristics, along with a description of the experimental procedure employed during the experiments on the various DIII-D tiles.

2.1 Experimental Facility

The main components of this low energy ion gun facility include the vacuum chamber, ion gun and mass filter system, deceleration lens, quadrupole mass spectrometer, and data acquisition system; refer to figure 11. Samples are mounted in the main vacuum chamber on a linear motion feedthough device which allows for vertical movement of the sample, perpendicular to the incident ion beam. The sample is heated resistively and its temperature is measured by optical pyrometry.

2.1.1 UHV System

The entire UHV facility is pumped by a 360L/s Leybold-Heraus turbomolecular pump backed by a Leybold Trivac mechanical pump. The main test chamber is equipped with several ports of various dimensions. The sample is held in place by stainless steel jaws and positioned roughly in the centre of the test chamber, normal to the incident ion beam.

Prior to running chemical erosion experiments, it is necessary to condition the UHV system. After exposure to atmosphere, the entire system is baked at ~500 K for at least 24 hours, resulting in base pressures $< 10^{-9}$ torr, consisting mainly of D_2 and CO, with smaller contribution from H_2O and CO_2. To further reduce water levels and to reduce signal confusion due to deuterated hydrocarbons undergoing isotope exchange on the chamber walls, a hot tungsten ring filament is run for another 24 hours producing D^0 atoms in a deuterium backfill of $\sim 10^{-4}$ torr.

2.1.2 Ion Gun and Mass Filter

A SPECS IQE 12/38 electron impact extraction type ion gun in conjunction with a SPECS Wein-type mass filter are used to create an exclusively D_2^+ ion beam. The ion source consists of a chamber containing an anode cage enclosed by an iridium coated ring filament cathode. A high density of D_2^+ ions is created in this region by 100 eV electrons emitted from the ring filament and traversing the anode cage numerous times. These ions are then extracted from the ionization chamber at selectable energies between 0.2 and 5 keV. These ions subsequently enter the Wein mass filter, which employs an $\vec{E} \times \vec{B}$ force to select ions at a specific velocity. There is also a 2 degree bend in the filter so that only ions with

the prescribed radius of curvature pass through, keeping the beam free of neutrals. The final stage of the ion gun/mass filter pair is two electrostatic lens elements, which allow for variable focussing of the beam.

In order to ensure that the ion beam was roughly monoenergetic, ion beam energy spread analysis measurements were made using a four stage energy analyzer. These measurements were used to determine the optimum operating conditions of the ion gun, maximizing current while minimizing the energy spread in the beam. It was found that stable currents ($\sim$ 2.5 - 3.0 μA) with minimal energy spread ($\sim \pm 5$ eV) could be achieved with initial ion energies of $\sim$ 1000 eV and main chamber pressures of $\sim$ 7.5 - 9.0 $\times$ 10^{-7} torr. The plasma potential offset in the ion gun was found to vary depending on the operating conditions, but was optimally $\sim$ 30 V.

2.1.3 5-Element Electrostatic Deceleration Lens

A 5-element cylindrically symmetric lens, using the target as an additional end electrode (designed by Mech [20]) was used to decelerate the beam of mass selected D_3^- ions. For this lens configuration, the final ion energy is the difference between the initial beam energy and the bias applied to the target. In this experiment, ions were decelerated to energies of 50 eV/D^+ and 200 eV/D^+, with a beam flux of 1 - 1.5 $\times 10^{18} D^+/m^2 s$ over an eliptical spot of $\sim$ 4 $\times$ 6 mm dimensions ($\sim$ 20 mm^2 area).

2.1.4 Quadrupole Mass Spectrometer and Data Acquisition

Chemical erosion reaction products are monitored in the residual gas using an Extranuclear quadrupole mass spectrometer (QMS). Due to the varying quadrupole sensitivity to the background deuterium pressure, it is necessary to ensure that the backgroud pressure remains nearly constant during chemical erosion experiments. The QMS is calibrated *in-situ* with known leaks of CD_4, C_2D_4, and C_3D_6. Relative sensitivities for C_2D_2, C_2D_6, and C_3D_8 are estimated from previous calibrations [37].

Computer-controlled data acquisition is performed employing a 16 bit National Instruments ATMIO16 board and the LabWindows user interface environment. This allows for measurements of signal intensity for selected quadrupole masses, along with display, handling and storage of erosion measurement data. The erosion product spectrum analysis is made using matrix analysis techniques, which are elaborated on in section 2.3.2.

2.1.5 DIII-D Tile Samples

Two samples from the DIII-D tokamak were investigated, one from the outer midplane region and one from the lower inner divertor. Both tile samples were UCAR-TS-1792 (ATJ) graphite, and were present in the tokamak through the 1993–1999 operational period. The outer midplane sample, which was more extensively studied at UTIAS, has a distinct reddish coloring when viewed from straight on, and is speckled and non-uniform in appearance. The

sample from the lower inner divertor is of a blueish-grey hue, and is streaked with arc tracks from tokamak operation (see figure 12).

2.2 Experimental Procedure

All chemical erosion experiments of DIII-D tile samples were performed in the UHV system described above. Following system conditioning (system bake and H^o impact on the chamber walls), it was necessary to establish a "conditionning spot" on the sample in order to stabilize the ion gun performance. The ion gun was run on this spot prior to the acquisition of each data set in order to ensure steady equilibrated background sytem conditions. A new spot location was used for each new experiment, eliminating effects of damage due to prior irradiation.

The experimental set performed on the mid-plane tile sample MP3 was conducted at two selected ion energies (50 eV and 200 eV), and three temperatures (300 K, 500 K and 700 K), roughly approximating a broad range of operating conditions in the DIII-D tokamak. The chemical erosion yield of methane and heavier hydrocarbons (C_2D_2, C_2D_4, C_2D_6, C_3D_6, and C_3D_8) was determined as a function of the incident ion fluence. The sample temperature was measured by optical pyrometry, and ion energies were measured as the difference between the extracted beam energy and the sample bias potential. Since the transmitted ions are molecular, this energy is divided between the atoms in the molecule and may vary by a few eV (on the order of the molecular binding energy) in the case of uneven sharing of energy as the molecule strikes the sample surface. In this thesis, D^+ is used to distinguish incident particles, however, it should be noted that deuterium atoms in the D_2^+ beam are neutralized upon impact.

Prior to each experiment, the quadrupole sensitivity was calibrated *in-situ* against known leaks of CD_4, C_2D_4, and C_3D_6. The experiment began with the selection of a new beam spot location. QMS signals for all masses[1] were scanned and recorded by the data acquisition system. Each mass peak was scanned three times in a step-wise (5 steps) fashion. A typical mass spectrum showing the relative contributions of the leak bottles is shown in figure 13. The maximal signal value was then selected and displayed in a real-time plot. The final value of the mass signal was then taken as an average of between 30-50 of these maximal values. The number of values averaged in each measurement depended on the signal stability, and was usually an average of 50 points.

Once the ion beam was turned on to the new spot, the evolution of the chemical erosion signal was plotted in real-time and displayed on the data acquisition (DAQ) computer system. Measurements were made at roughly equal fluence intervals, approximately every hour (depending on the beam current), with the first data point taken after half an hour of running on the new spot. Subsequent to each data point measurement, the ion beam was turned off and another signal measurement was taken when background steady-state was achieved, in order to account for any drift in the background signal. The difference in the

[1]The erosion signals for masses 12–52 were recorded.

"beam on" and "beam off" signals was then taken as the measured erosion signal. Figure 14 shows a typical trace of the raw data for masses 18, 26, and 32.

2.3 Analysis of Erosion Signals

Calculation of the actual erosion yields in these experiments is complicated by: (1) the variance in the QMS sensitivity to each of the hydrocarbon species, (2) the QMS convolution of the measured signals due to hydrocarbon cracking in the ionizer, and (3) wall contributions due to hydrocarbon formation from reflected deuterium ions incident on the wall surface. These issues are addressed below.

2.3.1 Relative QMS Sensitivities

Using the matrix analysis of chemical erosion signals described by Davis [37] it is possible to define six principal analysis masses. Each of six hydrocarbon species (CD_4, C_2D_2, C_2D_4, C_2D_6, C_3D_6, and C_3D_8) is assigned a principal analysis mass. Table 2.1 summarizes the assignments for D^+ irradiation.

Hydrocarbon Species	Analysis Mass (*amu*)
CD_4	18
C_2D_2	26
C_2D_4	32
C_2D_6	36
C_3D_6	46
C_3D_8	34

Table 2.1: Principal masses used for analysis for D^+ irradiation experiments.

Using three in-situ leak bottles, it is possible to determine the relative QMS sensitivity for ethylene (C_2D_4) and propene (C_3D_6) with respect to methane (CD_4). The relative sensitivities of the other three principal masses were estimated based on the previous results of Davis [37]. Relative sensitivities to methane were measured prior to each set of experiments, and did not vary significantly ($< 5\%$) between experiments. Table 2.2 shows a typical set of QMS sensitivities relative to methane.

2.3.2 Matrix Analysis of Erosion Signals

The determination of the chemical erosion yield is further complicated by the QMS convolution of the measured signals due to hydrocarbon cracking in the quadrupole ionizer. To account for the cracking of the heavier hydrocarbons, the cracking contributions to each of the six analysis masses was determined. It was possible to determine the exact cracking

Hydrocarbon Species	Relative Sensitivity
CD_4	1.00
C_2D_2	3.21
C_2D_4	1.11
C_2D_6	0.80
C_3D_6	1.05
C_3D_8	0.81

Table 2.2: Relative sensitivities of principal masses used for analysis of various hydrocarbon species to methane.

patterns of three of the six anlysis masses with the three in-situ leak bottles: the other three cracking patterns were inferred from the results of Davis [37]. From these results, a 6×6 cracking pattern matrix can be formed with columns representing the six hydrocarbon species in ascending mass order and the rows being the principal analysis masses in ascending numerical order. Below is a tyipical example of the cracking pattern matrix used in the calculation of the erosion yields.

$$\mathbf{C} = \begin{bmatrix} & CD_4 & C_2D_2 & C_2D_4 & C_2D_6 & C_3D_6 & C_3D_8 \\ 18 & 1 & 0 & 0 & 0 & 0.191 & 0 \\ 26 & 0 & 1 & 0.126 & 0.038 & 0.075 & 0 \\ 32 & 0 & 0 & 1 & 1 & 0.021 & 0.717 \\ 34 & 0 & 0 & 0 & 0.203 & 0 & 1 \\ 36 & 0 & 0 & 0 & 0.187 & 0 & 0 \\ 46 & 0 & 0 & 0 & 0 & 1 & 0.060 \end{bmatrix}$$

If we define the measured signal vector divided by the incident ion flux as $\vec{s}$, and given the cracking matrix $\mathbf{C}$, the relative sensitivities to methane in a 6×6 diagonal matrix, Υ, and the QMS sensitivity to methane, κ, then

$$\mathbf{C}\vec{y} = \kappa\Upsilon\vec{s}$$

We can now determine the erosion yield vector

$$\vec{y} = \kappa\mathbf{C}^{-1}(\Upsilon\vec{s})$$

The hydrocarbon erosion yield can now be determined given the measured erosion signal from each of the six principal analysis masses.

2.3.3 Wall Contribution to Erosion Signals

When performing ion beam chemical erosion experiments with graphite, a fraction of the incident deuterium ions are reflected from the target surface to the walls of the vacuum system. Here they can form hydrocarbon molecules which are subsequently desorbed and detected by the RGA. This component of the erosion signal is called the wall contribution, and must be subtracted from the measured erosion signal in order to determine the actual chemical erosion yield from the sample surface. Wall contributions are measured using the procedure in [20]. The sample is initially annealed at 1200 K for ~10 seconds in order to thermally desorb the deuterium from the sample, followed by a cooling period of ~45 minutes. The ion beam is then turned on. Typically, a very fast rise in the methane signal is measured (see the "beam on" arrow in figure 15), followed by a slower increase. If we assume that there is 100% retention of the non-reflected particles, we can calculate the fluence corresponding to the saturation of the implantation zone, accounting for the difference in depth of the implantation zone with incident ion energy. For 50 eV D^+ impact on carbon, the incident fluence needed to saturate the implantation zone is $\approx 1.4 \times 10^{20} D^+/m^2$ [38], from which we can calculate the time required to reach saturation (assuming an incident flux of $\sim 3 \times 10^{18} D^+/m^2 s$) to be ~45 seconds. This implies that the initial step in the hydrocarbon signals cannot be due to hydrocarbon release from the sample since it is not completely hydrogenated. However, because hydrocarbon precursors exist on the vacuum vessel walls (resulting from the carbon sputtering history within the system), this nascent signal can be attributed to the interaction of the reflected D with the inner vessel surfaces.

In the present experiments with the DIII-D tile samples, these contributions had to be estimated because an initial anneal at 1200 K would have damaged the films on the sample surfaces. Wall contributions were estimated after performing the erosion measurements at 700 K (the highest temperature studied in these experiments). Following the 700 K measurements, the sample was left to cool to ~300 K, whereupon the ion beam was turned on. The prompt rise in the measured erosion signal was taken to be the wall contribution. The measured value of the wall contribution was typically <20% of the total erosion signal, i.e., the sum of the measured hydrocarbon $C_x D_y$. In the case of methane alone, the measured wall contribution was <5–10% of the methane signal. The uncertainty in these wall contribution measurements represents the main component of error in the erosion yield values.

3 Experimental Results

This section presents the results of the chemical erosion experiments on two DIII-D tile samples; MP3 from the outer midpane region, and B3 from the lower divertor region. Also presented here are results from surface analyses performed on the tile samples in order to substantiate the ensuing discussion.

3.1 Midplane Sample MP3

3.1.1 Surface Analysis

Numerous surface analysis methods were performed on the MP3 tile sample in order to characterize the film present on its surface. The techniques employed, along with the major observations are presented here.

Scanning Electron Microscopy (SEM)

SEM photographs of the sample were made both of the surface and in cross-section by Fred Neub of the Department of Material Science at the University of Toronto. Photographs of the surface (figure 16 a)) show a globular structure, which is typical for plasma-deposited films. Figure 16 b) shows an SEM photograph of the same sample in cross-section. The top surface, the film layer and the carbon substrate are all clearly visible in the photo, and the film thickness can be estimated to be ~1–2 μm.

Energy Dispersive X-Ray Spectroscopy (EDX)

EDX analysis spectra were provided by Fred Neub of the Department of Materials Science at the University of Toronto. Within the EDX analysis zone (~2–3 μm), an EDX spectrum of the midplane sample indicate trace amounts of aluminum, silicon, sulpher, calcium, and copper, as well as a few at% carbon, nitrogen, and oxygen. The remainder of the film (~90 at%) is interpreted to be boron, indicating that the layer consists mostly of boron extending to at least 2–3 μm (see figure 17). It should be noted that EDX has a *very* low sensitivity to boron, and the relative heights of the peaks in the spectrum have no bearing on actual at% values. The amount of carbon found in this region, ~5–10 at%, is consistent with the amount of carbon deposited with the boron during the boronizations in DIII-D [35, 39].

X-Ray Photoelectron Spectroscopy (XPS)

XPS analysis is useful for garnering information in the near surface, and can provide information about atomic bonding in addition to compositional information within the first few monlayers. XPS analysis was performed by Dr. R.N. Sodhi of the University of Toronto

Centre for Biomaterials on the surface layer, as well as at two separate depths, following periods of Ar^+ sputtering. Only rough estimates of the sputter depths are available, since it was not possible to measure the sputtering beam current; the depths are estimated to be ~10 nm and ~75 nm. Table 3.1 summarizes the composition of the surface as determined by this method, prior to D^+ exposure.

	B at%	C at%	O at%	N at%	B/C
Front Surface	34	43	19	3-4	0.8
Depth ~10 nm	56	23	17	3-4	2.4
Depth ~75 nm	63	19	15	3-4	3.3

Table 3.1: Surface composition of tile sample MP3 by XPS analysis.

The boron bonding was mainly B–B in all three locations of measurement. In the virgin near surface, prior to Ar^+ sputtering, there was evidence of B–C and B–OD bonding. For the two sputtered depths, there was an increasing B–O component, and the B-C and B-OD components disappeared. Similarly, the carbon bonding is primarily found in C-C bonds. The type of carbon bond, however, seems to change after sputtering. Hydrocarbon bonds also account for a small amount of the carbon bonding. Surface oxygen is found in oxygenated hydrocarbons, with an increase in the B–O component observed after sputtering.

Secondary Ion Mass Spectroscopy (SIMS)

SIMS compositional depth profiles were generated by Cindy Huctwith at Surface Science Western, providing information within the first few monolayers of the surface (figure 18). The profiles in this figure do not represent the relative concentrations since the SIMS yields are not calibrated. A deuterium profile of a D^+-implanted pure carbon reference (HPG99 pyrolytic graphite form Union Carbide) was used to estimate the SIMS sputtering rate to be $\approx$ 3 nm/s.

The SIMS profile in figure 18 shows boron, carbon, oxygen, and deuterium components in the film. In the first 10 nm of the film there is an increasing signal from both the boron and deuterium components, which is consistent with the XPS results for boron, where in the first ~10 nm the B concentration increased from 34 at% to 56 at%. The carbon component in the film is seen to extend to a depth of >30 nm, however, no surface peak is observed as in the XPS spectrum. Changes in the sensitivities due to variations in the surface potentials in the first few nm of the matrix, leading to large changes in the signal sensitivity, may be responsible for the strong increase in all signals immediately at the surface. This effect could also obscure a decrease in the carbon concentration with depth from the film surface. The B/C ratio is also seen to increase by a factor of 4 between 30 seconds (~1 nm) and 300 seconds (~10 nm) of sputtering. This is consistent with the results from the XPS analysis, which indicates a factor of ~3 increase in the B/C ratio from 0.8 B/C at the surface to 2.4 B/C at ~10 nm.

Summary

It can be concluded from the various surface analyses that the MP3 tile sample has a thick layer of plasma-deposited boron on the surface of the UCAR-TS-1792 (ATJ) graphite substrate, introduced during the numerous boronizations during the operation of the DIII-D tokamak. The thickness of this boron layer (~2 μm) is consistent with the amount of boron deposited on the inner vessel wall of DIII-D (~ 3 - 5 μm averaged over the entire surface area [35, 39]) during these boronizations. On the surface of this boron layer is a thin layer of an amporphous B/C:H film containing aproximately 20 at% carbon. This surface carbon layer indicates that the midplane surfaces are areas of net carbon deposition in the tokamak, at least for some part of the discharge.

3.1.2 Chemical Erosion Due to D^+ Impact

Chemical erosion experiments have been performed for 50 eV and 200 eV/D^+ impact at sample temperatures of 300 K, 500 K, and 700 K. Figures 19 and 20 show the methane and total carbon ($\sum C_i D_j$) erosion yields for 50 eV and 200 eV D^+ irradiation, respectively, as a function of fluence. It can be seen for the midplane tile sample that the general trend in the fluence dependence is similar for all temperatures and energies.

Low Temperature Chemical Erosion Results (T~ 300 K)

At a temperature of 300 K, erosion yields are initially the same as that of the pyrolytic graphite (0.01–0.015 C/D^+) [40], but yields are seen to decrease by a factor of about two with increasing fluence. It should be noted, however, that in order to obtain these fluences, experiments were performed over the course of several days. In each new day of experiments, the first yield measurement made was a factor of ~1.5 times high, but slightly decreasing with each new day. This may be attributed to carbon segregation to the sample surface between each run, or may also be a conditioning effect when the beam is turned on to the sample spot after the initial calibration measurements are made.

High Temperature Chemical Erosion Results (T≥500 K)

As the sample temperature is increased, yields are marginally increased, and are found initially to be factor of ~2 lower than that for pure graphite at 500 K [40], and a factor of ~4 lower than pure graphite at 700 K [40]. These yields are also seen to decrease by a factor of 1.5–2 as the fluence is increased. The erosion yields then level off and remain approximately constant (up to fluences of ~$8.5\times10^{22} D^+/m^2 s$ in the 50 eV and 500 K case). It should also be mentioned that the first experiment conducted was at 50 eV and 500 K, and the shift in the curves in figure 19 for this case is due to an uncertainty in the fluence measurement caused by changing beam operating conditions upon initiation of the experiment.

3.1.3 Discussion

The initial (i.e., at low fluence) erosion yields measured on the MP3 tile sample are similar to those found for doped graphites [26, 28]. At lower energies and temperatures, the yields are comparable to that of pure graphite, but are substantially lower at higher energies (200 eV) and temperatures (700 K). As the fluence is increased, the decrease in yield might be attributed to preferential removal of carbon from the film, leading to a boron enriched layer at the surface (see figure 12). The chemical erosion yield measurements, however, reach a steady state value with increasing fluence, but do not decrease to zero. This may imply that the erosion is limited by carbon diffusing to the film surface or by the removal of boron. Although no boron-containing molecules were detected in the QMS spectrum during the erosion measurements, the sensitivity to boron-containing molecules may be very low, or signals may be obscured by hydrocarbons. The increase in steady-state yield with sample temperature suggests that carbon diffusion through the a:B/C film may play an important role.

These results may at first appear to be inconsistent with the spectroscopic measurements made in DIII-D at the outer midplane. However, since the midplane surfaces experience incident D^+ fluxes of $\sim 4 \times 10^{20} D^+/m^2 s$ [42], for the shots which are ~ 5 s long the total fluence in this region is $\approx 2 \times 10^{21} D^+/m^2$. Based on the results of this study, the DIII-D fluence during a typical shot appears to be insufficient to remove the surface carbon layer. As a result, DIII-D erosion measurements over the course of a single discharge may match those of virgin or boron-doped graphite.

3.2 Inner Divertor Sample B3

The DIII-D divertor tile samples were split into nine fragments (see figure 21), with the toroidal angle increasing from left to right, and the radial or outboard direction from bottom to top. Sample B3 was situated on the inner divertor side and would be subject to a wide range of plasma conditions. Generally, it would be exposed to the private flux, and could be either a region of net erosion or net deposition.

3.2.1 Surface Analysis

As with the midplane tile sample, various surface analysis techniques were used in order to characterize the surface of the lower divertor tile sample B3. The analyses were performed by those individuals/organizations mentioned in Section 3.1.1: Rutherford backscattering analysis, not mentioned in 3.1.1, was performed by Rick Macauley-Newcomb using facilities at the University of Western Ontario.

Scanning Electron Microscopy (SEM)

SEM photographs were taken of the surface of the B3 tile sample (see figure 22). The surface appears to be uniform and cracked, but fairly typical for a plasma deposited film.

Energy Dispersive X-Ray Spectroscopy (EDX)

The EDX spectra show that within the analysis zone (2–3 μm), there is primarily carbon, with 1–2% oxygen (and by inference boron), and trace amounts of aluminum, silicon, sulphur, chlorine, potassium, calcium, chromium, iron, and nickel. This is consistent with an area of net erosion (primarily carbon), with evidence of some redeposition (evidence of small boron concentrations).

X-Ray Photoelectron Spectroscopy (XPS)

XPS analysis was performed on the surface layer, as well as at a depth of ~5 nm after a short sputter. Table 3.2 summarizes the composition of the surface as determined by this method, prior to D^+ exposure. The XPS measurements show that the surface is composed almost exclusively of carbon. A small amount of boron (~3–5%) observed at the surface was reduced by ~50% after a very short sputter.

	B at%	C at%	O at%	N at%	B/C
Front Surface	3.0	77.4	17.3	2.3	0.040
Depth ~5 nm	1.4	92.1	5.4	1.2	0.015

Table 3.2: Surface composition of tile sample B3 by XPS analysis.

Rutherford Backscattering Analysis (RBS)

Results from RBS analysis are summarized in table 3.3. The boron results quoted here are upper limits, averaged over a depth of ~20 nm. These results are consistent with those found from EDX analysis, however the RBS signal could be interpreted as there being no boron present at all.

	C at%	O at%	B at%	Si at%	Ni at%	Mo at%
Front Surface	78	11	<11	<1	0.3	0.04
Averaged ~20 nm	88	6	<6	—	—	—

Table 3.3: Surface composition of tile sample B3 by RBS analysis

Auger Analysis on Sample B5 (Performed at PISCES-B, UCSD)

Auger analysis was performed on inner divertor sample B5 at the UCSD PISCES-B Facility before and after exposure to a moderately high flux deuterium plasma in PISCES-B. The B5 sample was located near B3 in the divertor (see figure 21). The results are summarized in table 3.4 [42]. The divertor sample was biased at 30 V and subjected to a flux of

$\sim 8 \times 10^{22} D^+/m^2 s$ for about 10 minutes. The CD band was seen to drop substantially after a few minutes of plasma exposure, indicating that carbon was quickly removed from the surface, leaving a B rich amorphous boron-carbon film.

Sample B5	Pre-Exposure	Post-Exposure
Carbon	~ 90%	~ 10%
Boron	~ 4%	~ 55%
Oxygen	~ 4%	~ 32%
Nitrogen	Trace	Trace

Table 3.4: Surface composition of tile sample B5 by Auger analysis at UCSD PISCES-B

Summary

The picture provided for the surface of the inner divertor tile samples is a little convoluted. For the B3 sample, there exists a very thin amorphous boron-carbon plasma-deposited film on the surface, consisting mainly of carbon with small amounts of nitrogen, oxygen, and trace metals. The exact thickness of the film cannot be deduced from these results, but XPS and RBS analyses indicate it is likely in the range of ~5 - 20 nm. The PISCES-B analysis of sample B5 produced results similar to that of B3 at the surface, but found a primarily boron-containing film underneath. However, because of strong spatial flux gradients in the divertor region, it may be possible for substantially different surfaces to exist on fragments 3 and 5 of the same tile.

3.2.2 Chemical Erosion Due to D^+ Impact

Preliminary chemical erosion experiments were conducted on the inner divertor sample B3 at an incident D^+ energy of 50 eV, at temperatures of 300 K and 500 K. These experiments yielded only rough qualitative results, since background wall contributions could not be measured at these low temperatures. Figure 23 shows the erosion signal intensity as a function of fluence for methane, without deductions due to the wall contribution. Note that the "yield" values quoted could be up to ~50% high in the case of methane, since the wall contribution would be a constant deducted from all erosion signals.

These preliminary experiments indicate a general trend where at low fluence ($\leq 10^{21} D^+/m^2$), the erosion yield is lower than the steady-state yield achieved at higher fluences ($\geq 4 \times 10^{21} D^+/m^2$). These calculated "yields" are seen to be higher than that of graphite, although once wall contributions are accounted for, would be roughly in the graphite yield range. It was also observed that there is no evidence of any boron hydrides in the erosion spectra (although again, this may be a sensitivity issue). Upon visual examination of the sample, it is seen that the film has been completely eroded through to the graphite substrate (see figure 12). This effect was seen even on a spot that had only been exposed to the beam for ~1 hour, or a fluence of $\sim 4 \times 10^{21} D^+/m^2$.

3.2.3 Discussion

From these preliminary experiments, it appears that there exists an extremely thin deposited film on the surface of the graphitic substrate. With an incident beam current of $\sim 2.5\mu$A, the erosion rate can be estimated at $\sim 1 - 2$ nm/h, implying the film is only a few nanometers thick. This picture is generally confirmed by the surface analysis performed on the B3 sample. A general picture can be constructed for the erosion experiments. Initially, when the beam is first turned on the sample, the erosion yield is slightly lower than that of pure carbon. As the film is eroded away, the methane yield increases until the film is gone, leaving a steady-state erosion yield similar to that of graphite extending up to high fluences. The small scatter in the yield for fluences $< 4 \times 10^{21} D^+/m^2$ may indicate that there is some variability in the erosion yield across the film, with more loosely-bound carbon (and subsequently hydrocarbon precursors) existing at the interface between the film and substrate.

The inner divertor region of DIII-D is a mix of inner strike point (ISP), private-flux, and outer strike point (OSP) exposure, and the B3 position of the inner divertor is actually the position of the OSP during double-null plasmas. So, it appears that at the time of removal of this sample, this region was actually more like a net erosion or else a very weak redeposition region.

The present experiments have only been conducted at 300 and 500 K, which are below the temperatures required for the reduction of erosion yields seen in boron-doped graphites. It is possible that for temperatures >500 K, these effects will become more pronounced, and the initial yields may be lower than those measured here. However, at higher fluences, reduced yields should disappear with the departure of the film on the surface of the divertor tile substrate.

4 Conclusions

Spectroscopic data of chemical erosion in the DIII-D tokamak has been compiled over the past eight years, from which it was found that CD band emissions at the lower divertor, near the inner strike point have decreased by a factor of 10–20. At the outer midplane, however, erosion yields have remained static and similar to that of pure graphite. Pieces of divertor and midplane tiles from the DIII-D have been studied in controlled ion-beam experiments to determine their erosion characteristics under low energy deuterium impact (50 eV and 200 eV) as a function of fluence for sample temperatures of 300 K, 500 K, and 700 K.

Surface analysis of the outer midplane sample MP3 concluded that the surface primarily comprises boron, with a thin B/C overlayer. The initial chemical erosion yields were found to be consistent with that of boron-doped graphite, with total hydorcarbon ($\sum C_i H_i$) yields of $\sim 0.01 - 0.02 C/D^+$. The erosion yields were found to decrease by a factor of 1.5–2 with increasing fluence in the range of $\sim 4 \times 10^{21} - 3 \times 10^{22} D^+/m^2$. Erosion yields leveled off for fluences $\geq 3 \times 10^{22} D^+/m^2$. In DIII-D, with typical shot durations of ~5 s and fluxes of $\sim 4 \times 10^{20} D^+/m^2 s$ [42], the incident fluence of a single shot is $\sim 2 \times 10^{21} D^+/m^2$, and thus the erosion yield is expected to be similar to that of carbon for the duration of the discharge.

For the inner divertor sample B3, surface analysis showed very little boron on the surface, and at a depth of ~5 nm the sample was found to be primarily carbon. Chemical erosion yields for incident D^+ energies of 50 eV and sample temperatures of 300 K and 500 K were found to be comparable to that of pure graphite. Visual inspection indicated that the film was eroded through to the graphite substrate, even where the sample had been exposed to fluences as low as $\sim 10^{21} D^+/m^2$ at 300 K, confirming the observed chemical erosion results. In the region of the divertor from where this sample was removed, there has been a mix of ISP, private-flux, and OSP exposure, and during double-null plasmas, the B3 position of the inner divertor is actually the position of the OSP. It is probable that at the time of removal of this sample, this region was actually more like net erosion or else very weak redeposition. Thus, only a very thin film was detected on the surface, and the present measurement of chemical erosion yields are very similar to that of pure graphite.

References

[1] J. Edmonds and J. Reilly, *Global Energy: Assessing the Future* Oxford University Press, 1985.

[2] "The U.S. Program of Fusion Energy Research and Development" by the President's Committee of Advisors on Science and Technology, (Panel Chair John P. Holdren), July 1995.

[3] P. C. Stangeby, *The Plasma Boundary* IOP Publishing, Williston VT. 2000.

[4] P. C. Stangeby and G. M. McCracken, *Nucl. Fusion* **30** (1990), 1225.

[5] J. W. Davis and A. A. Haasz, *J. Nucl. Mater.* **241–243** (1997), 37.

[6] A. Kallenbach et al., *Nucl. Fusion* **34** (1994), 1557.

[7] K. Behringer, *J. Nucl. Mater.* **176–177** (1990), 606.

[8] C. S. Pitcher et al., *Nucl. Fusion* **26** (1986), 1641.

[9] A. Pospieszczyk et al., *J. Nucl. Mater.* **145–147** (1987), 574.

[10] C. C. Klepper et al., *J. Nucl. Mater.* **220–221** (1995), 521.

[11] V. Philipps, E. Vietzke, and M. Erdweg, *J. Nucl. Mater.* **162–164** (1989), 550.

[12] V. Philipps, E. Vietzke, and M. Erdweg, *Plasma Phys. Contr. Fusion* **31** (1989), 1685.

[13] E. Vietzke and A. A. Haasz in: *Physical Processes of the Interaction of Fusion Plasmas with Solids* eds. W. O. Hofer and J. Roth. Academic Press, Amsterdam. (1996), 135.

[14] C. Garcia-Rosales, *J. Nucl. Mater.* **211** (1994), 202.

[15] M. Balden and J. Roth, *J. Nucl. Mater.* **280** (2000), 39.

[16] J. Roth and J. Bohdansky, *Nucl. Instrum. Methods B* **23** (1987), 549.

[17] J. W. Davis, A. A. Haasz, and P. C. Stangeby, *J. Nucl. Mater.* **145–147** (1987), 417.

[18] C. H. Wu, J. W. Davis, and A. A. Haasz, *Proc. 15th European Conf. on Controlled Fusion and Plasma Heating*, Dubrovnik, May 16–20, 1988, Europhysics Conf. Abstracts Vol. 12B Part II, 691.

[19] E. Vietzke, K. Flaskamp, and V. Philipps, *J. Nucl. Mater.* **128–129** (1984), 545.

[20] B. V. Mech, *Hydrocarbon Yield of Pyrolytic Graphite due to Low Energy Hydrogen Irradiation*, Ph.D. Thesis (1997).

[21] J. W. Davis, A. A. Haasz, and P. C. Stangeby, *J. Nucl. Mater.* **155–157** (1988), 234.

[22] A. Annen, A. von Keudell, and W. Jacob, *J. Nucl. Mater.* **231** (1996), 151.

[23] A. Annen and W. Jacob, *Appl. Phys. Lett.* **71 (10)** (1997), 1326.

[24] K. Ohya et al., *Nucl. Instr. and Methods B* **153** (1999), 52.

[25] J. W. Davis and A. A. Haasz, *J. Nucl. Mater.* **175** (1990), 117.

[26] C. Garcia-Rosales and J. Roth, *J. Nucl. Mater.* **196–198** (1992), 573.

[27] A. Y. K. Chen, A. A. Haasz, and J. W. Davis, *J. Nucl. Mater.* **227** (1995), 66.

[28] J. W. Davis and A. A. Haasz, *J. Nucl. Mater.* **255** (1998), 214.

[29] O. Buzhinski and Y. Sements, *Fusion Tech.* **32** (1997), 1.

[30] U. Schneider et al., *J. Nucl. Mater.* **176–177** (1990), 350.

[31] J. Winter et al., *J. Nucl. Mater.* **162–164** (1989), 713.

[32] E. Gauthier et al., *J. Nucl. Mater.* **196–198** (1992), 637.

[33] H. F. Dylla et al., *J. Nucl. Mater.* **176–177** (1990), 337.

[34] G. Jackson et al., *J. Nucl. Mater.* **196–198** (1992), 236.

[35] D. Whyte et al., *J. Nucl. Mater.* 14th PSI, in press.

[36] T. C. Simonen, *Fusion Eng. Design* **39–40** (1998), 83.

[37] J. W. Davis, *Hydorgen Erosion of Carbon for Fusion Applications*, Ph. D. Thesis (1988).

[38] G. Staudenmaier et al., *J. Nucl. Mater.* **84** (1979), 149.

[39] K. L. Holtrop et al., *J. Vac. Sci. Technol. A* **15** (1997), 678.

[40] B. V. Mech, A. A. Haasz, and J. W. Davis, *J. Nucl. Mater.* **255** (1998), 153.

[41] M. R. Wade et al., *J. Nucl. Mater.* **220–222** (1995), 178.

[42] D. G. Whyte, General Atomics, San Diego, CA, private communication.

Figures

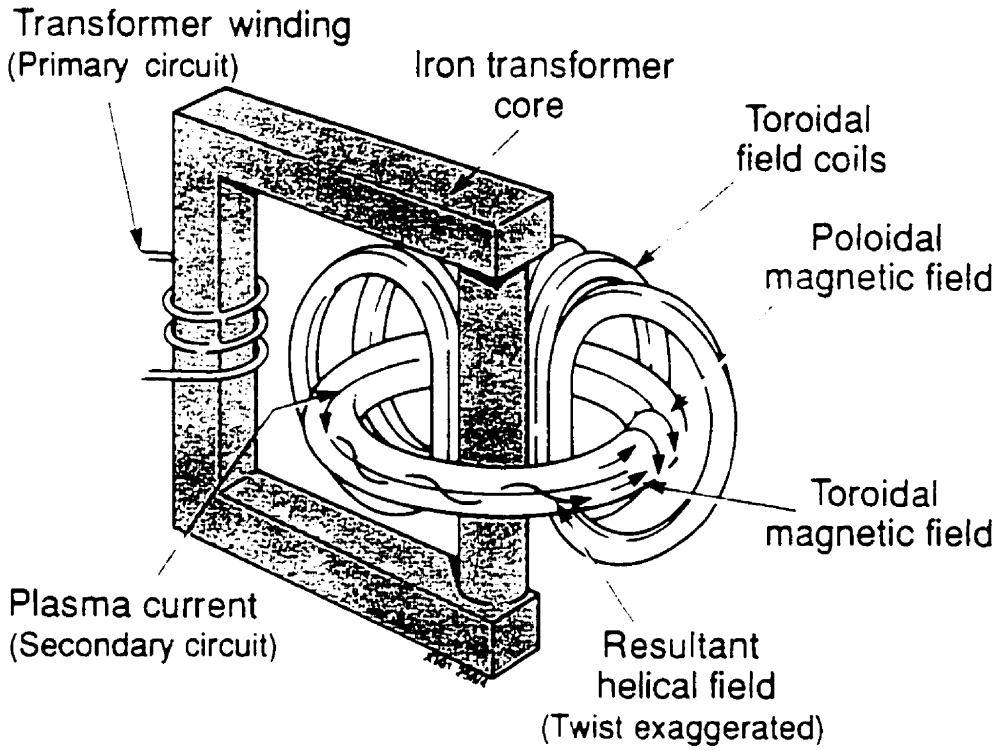

Figure 1: A tokamak magnetic fusion device.

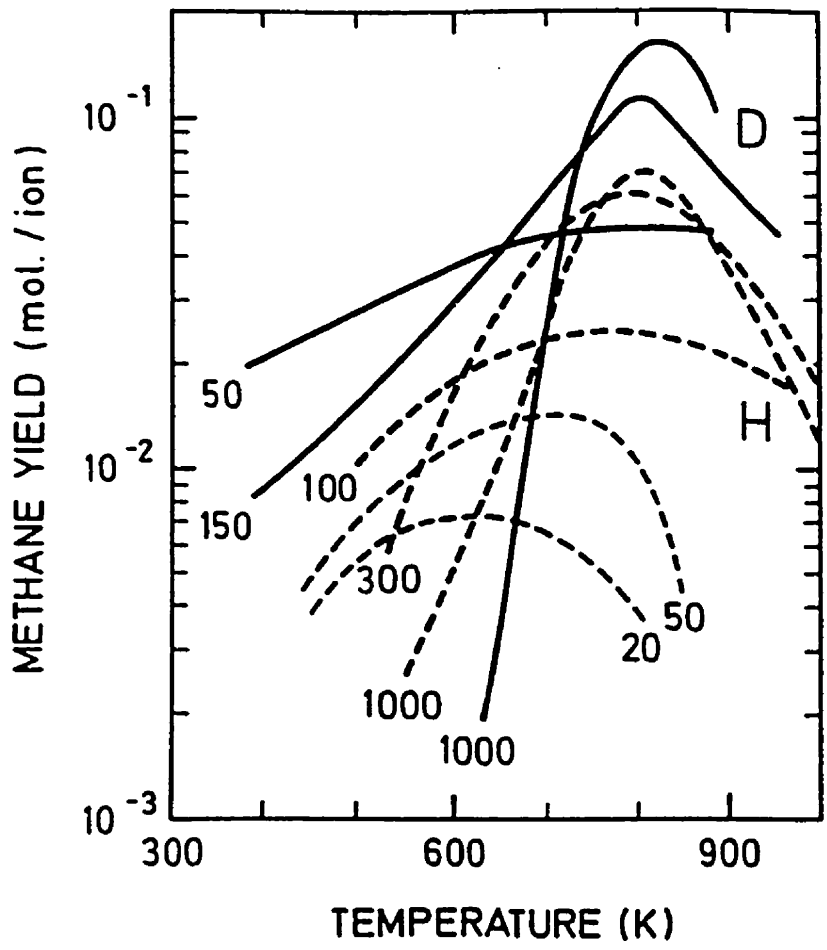

Figure 2: Chemical erosion yields of methane due to H^+ (dotted lines [17, 18]) and D^+ (solid lines [16]) irradiation of graphite as a function of temperature for energies of 50 eV - 1000 eV.

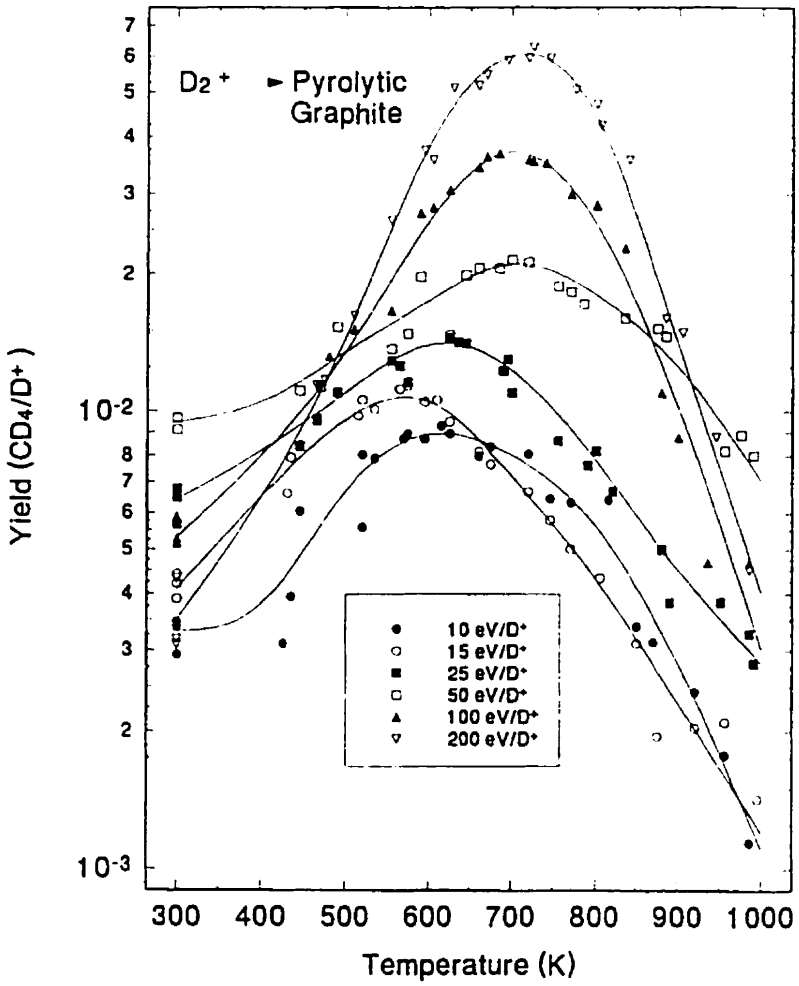

Figure 3: Methane yield due to D^+ irradiation of pyrolytic graphite as a function of temperature for energies of 10 eV - 50 eV [5, 20].

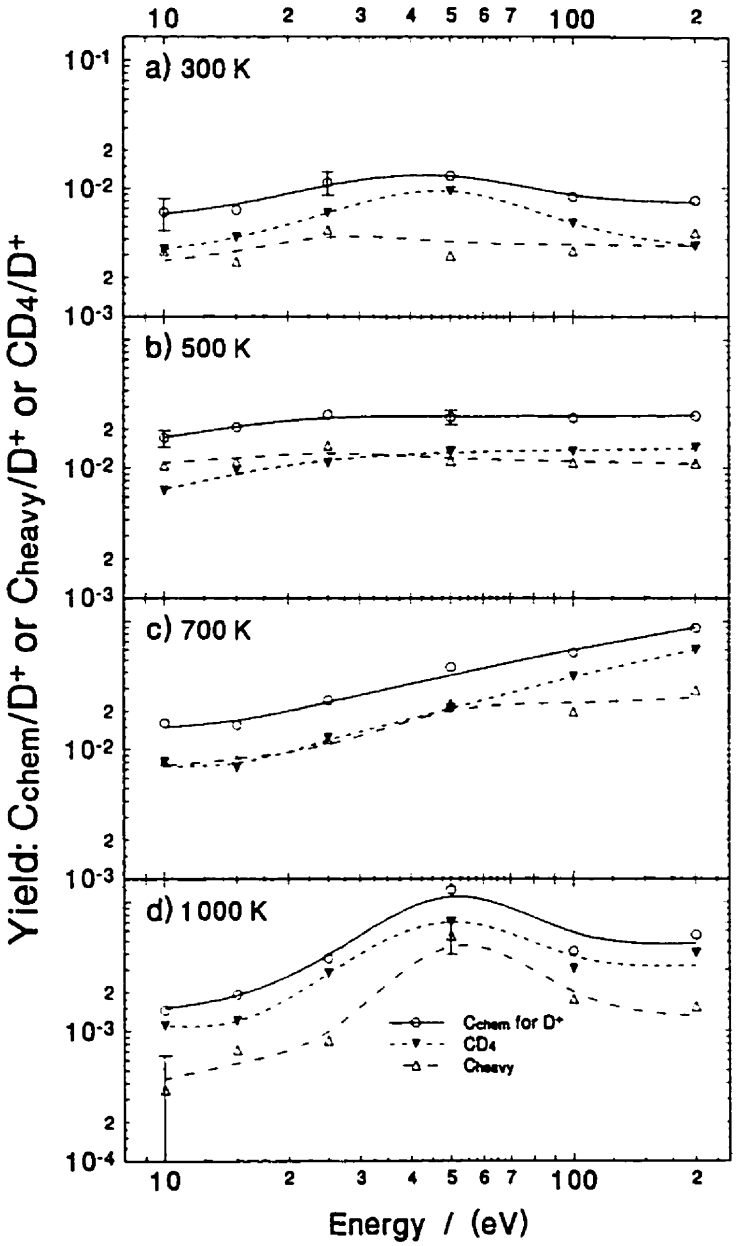

Figure 4: Methane, heavy hydrocarbon and total carbon yields of pyrolytic graphite as a function of ion energy for D_2^+ impact at a) 300 K, b) 500 K, c) 700 K, and d) 1000 K [20].

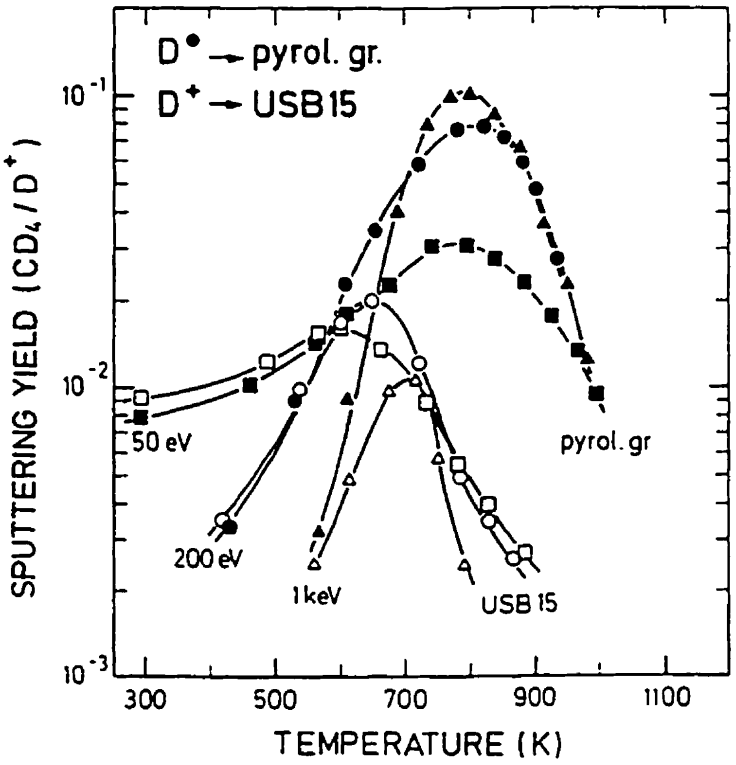

Figure 5: Methane yield for pyrolytic graphite (solid symbols) and USB15 (open symbols) as a function of temperature for D^+ at 50, 200, and 1000 eV impact [25].

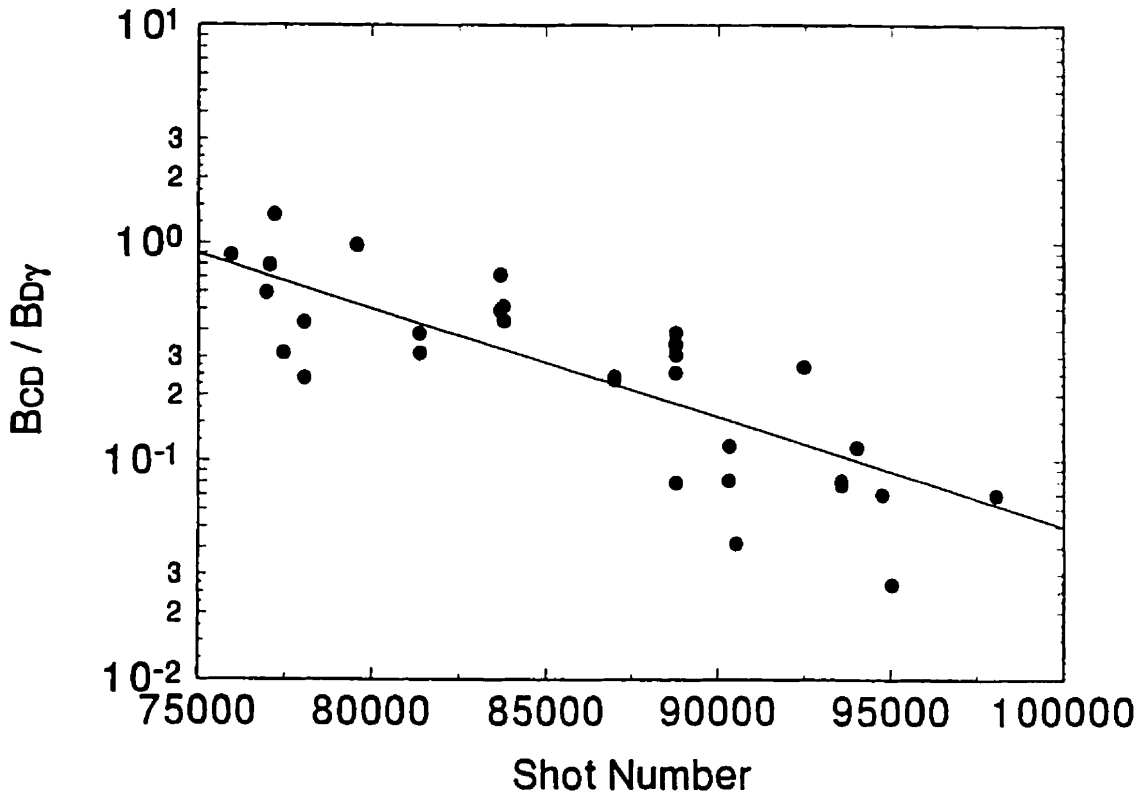

Figure 6: Reduction of the B_{CD}/B_{D_γ} ratio in the lower divertor region over the past ten years [34].

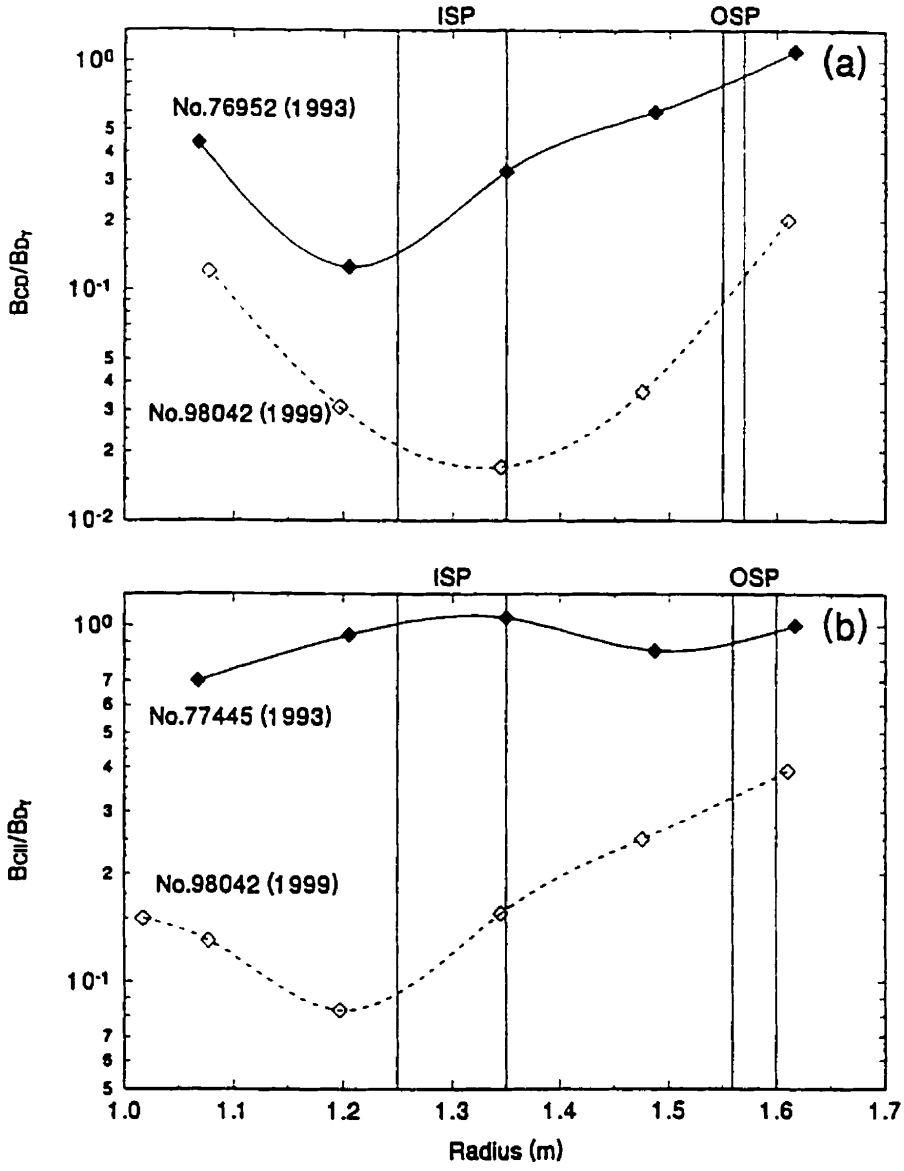

Figure 7: Comparison of (a) the B_{CD}/B_{D_γ} ratio and (b) the B_{CII}/B_{D_γ} for two nearly identical shots from 1993 and 1999 [34].

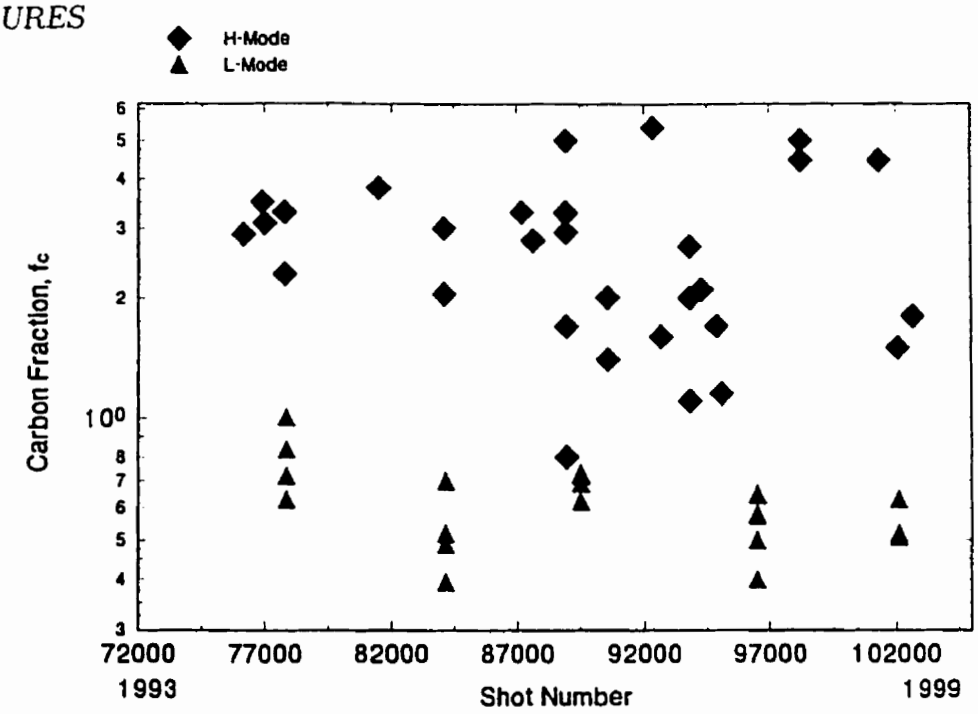

Figure 8: Core carbon fraction as a function of shot number for the operational period 1993 to 1999 [34].

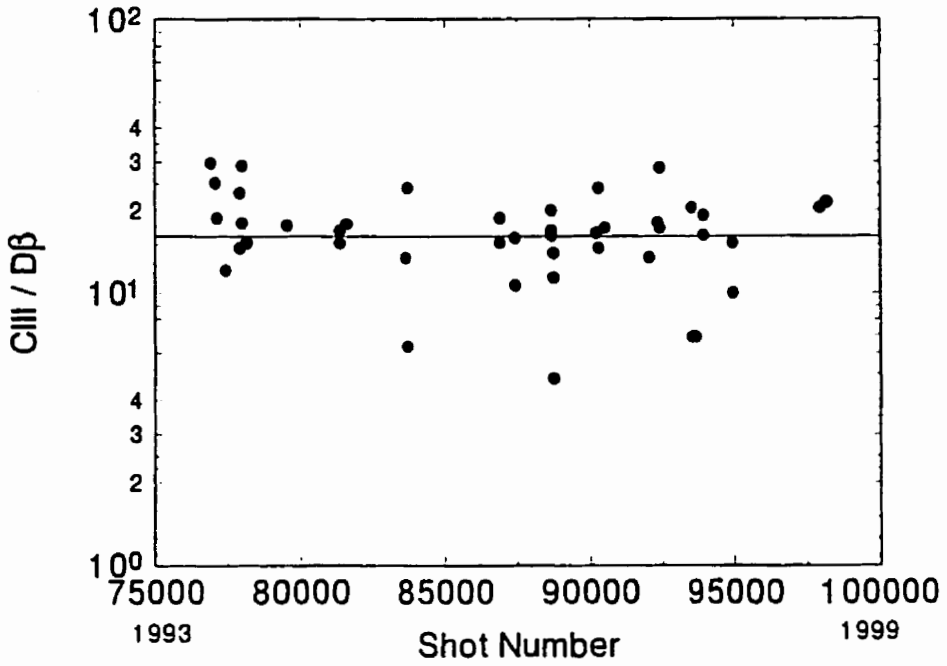

Figure 9: Midplane SPRED measurements from the outer midplane as a function of shot number from 1993 to 1999 [34].

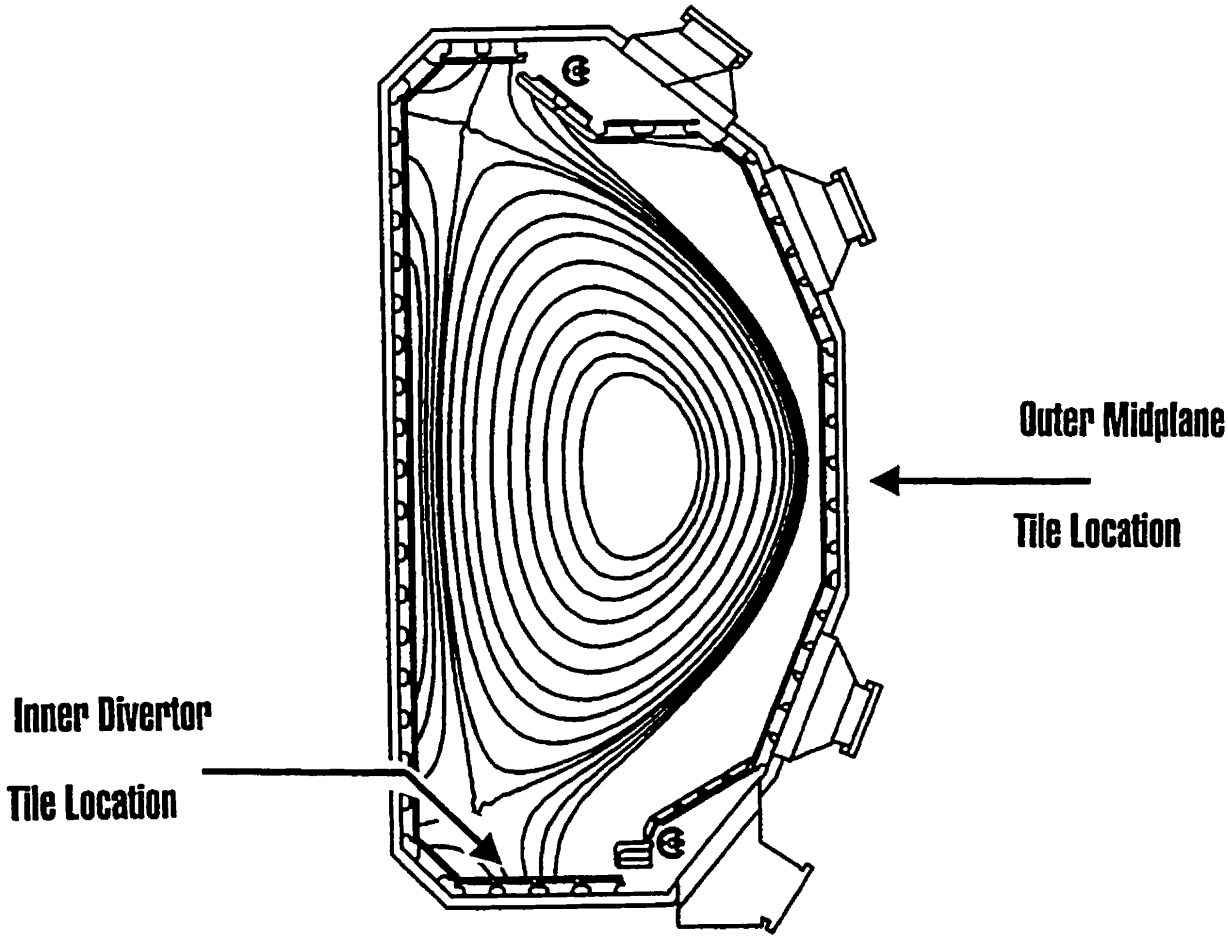

Figure 10: Cross-sectional schematic of the DIII-D tokamak indicating the location of the tile samples [35]. A more detailed sketch of the divertor tile region is shown in figure 21.

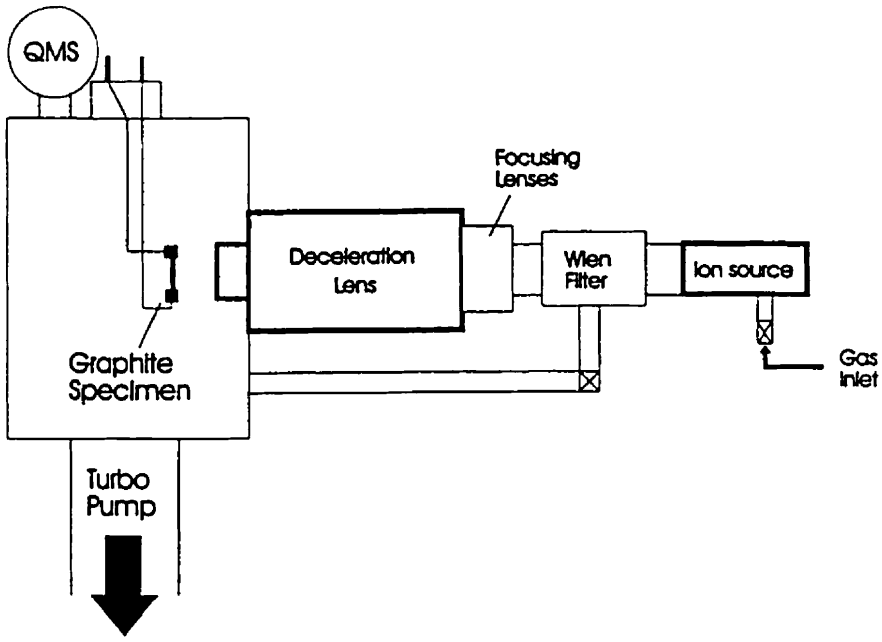

Figure 11: Schematic depiction of the experimental facility.

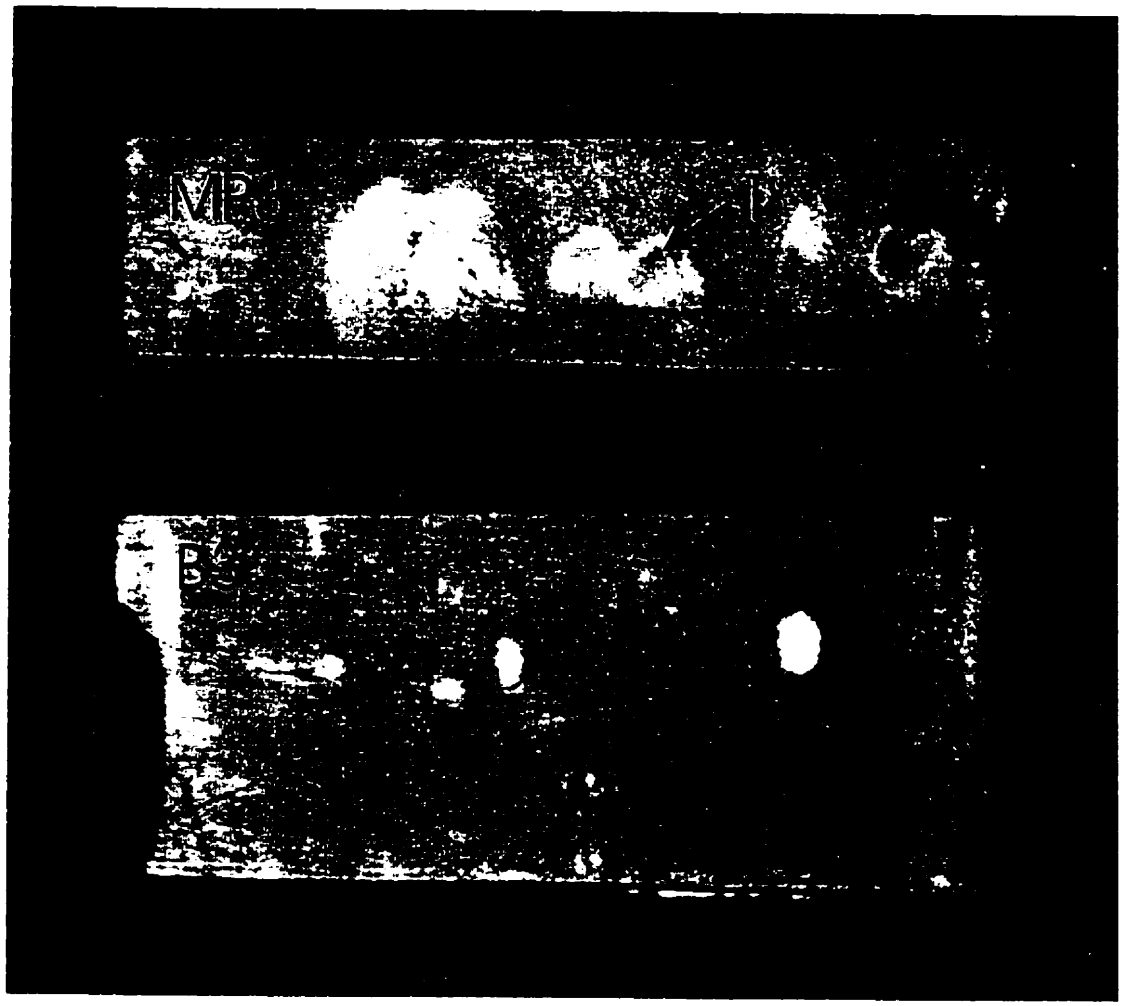

Figure 12: Digital photograph of midplane tile sample MP3 and divertor tile sample B3. Arrows (1) and (2) show the location of typical beam spots on the two samples.

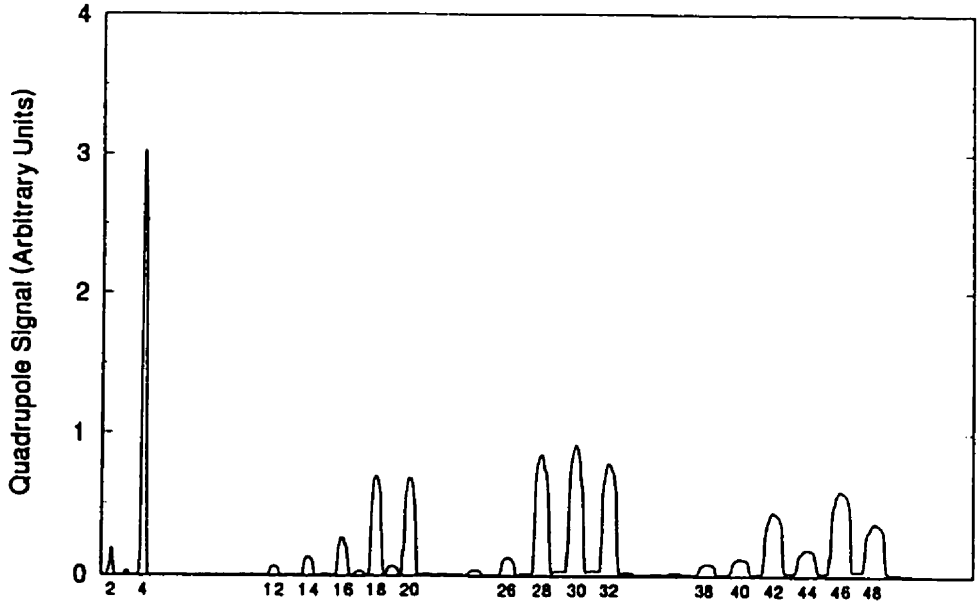

Figure 13: Trace of a typical QMS spectrum showing the relative contributions of the methane, ethylene and propene leak bottles.

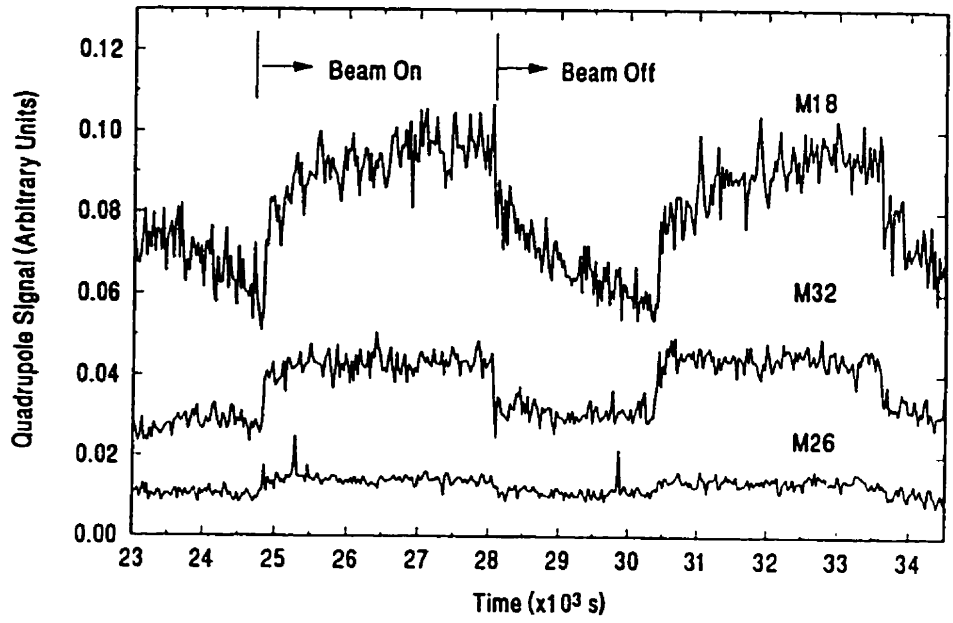

Figure 14: Trace of the "beam on" and "beam off" QMS signals for masses 18, 26, and 32.

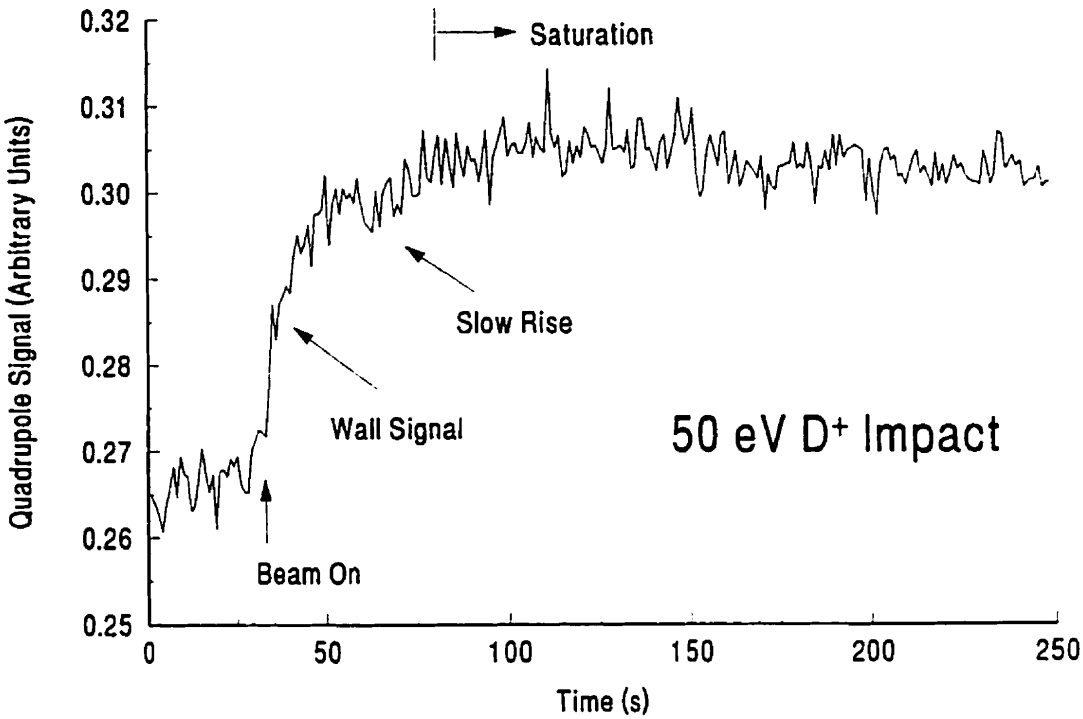

Figure 15: Rise in measured methane signal due to wall contribution from D^+ impact on midplane sample MP3. Following erosion measurements at 700 K, the specimen is left to cool to ~300 K. The ion beam is subsequently turned on, and the prompt rise in the measured erosion signal is taken to be the wall contribution.

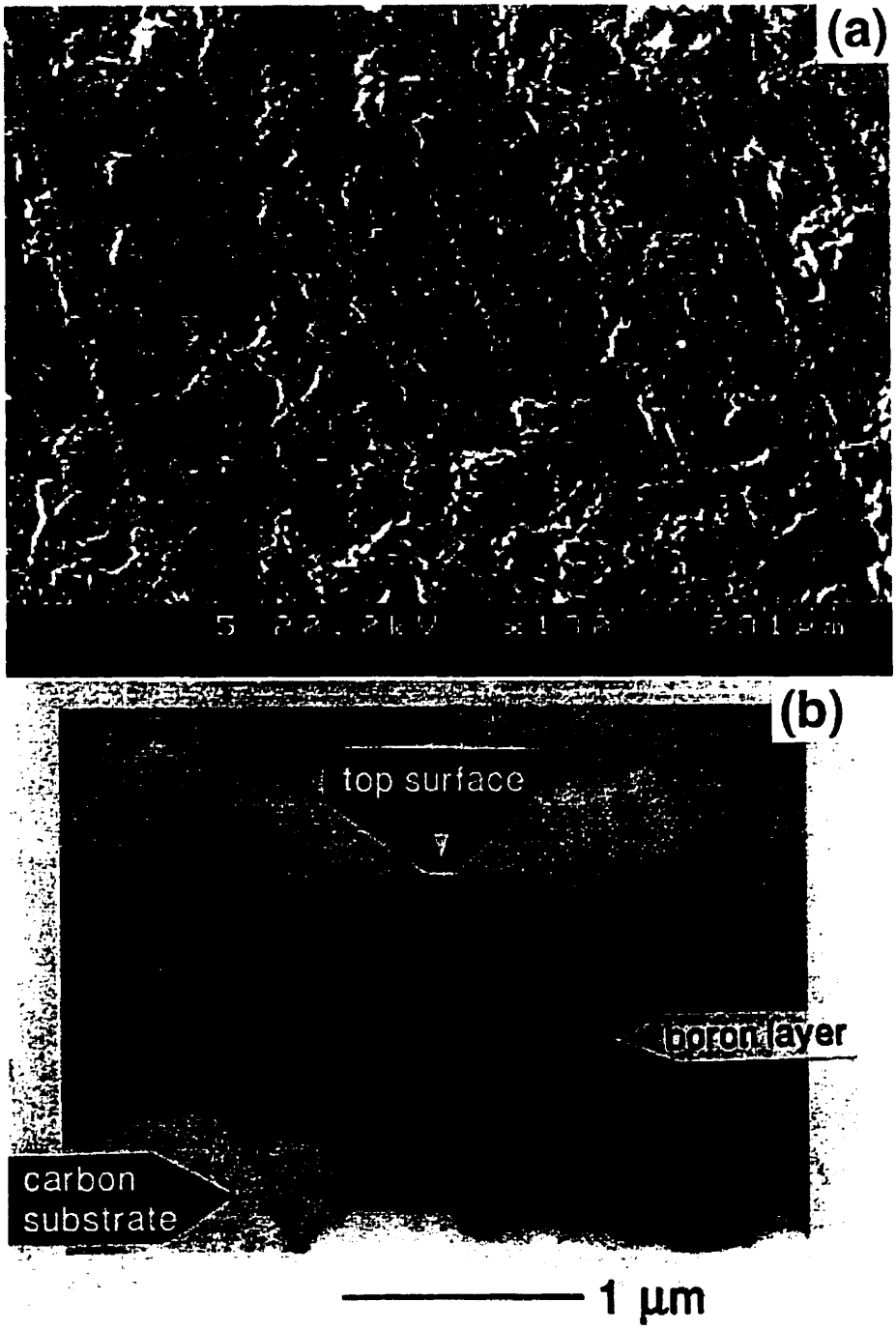

Figure 16: Scanning electron microscopy (SEM) photograph of (a) the MP3 sample surface and (b) of the MP3 sample cross-section

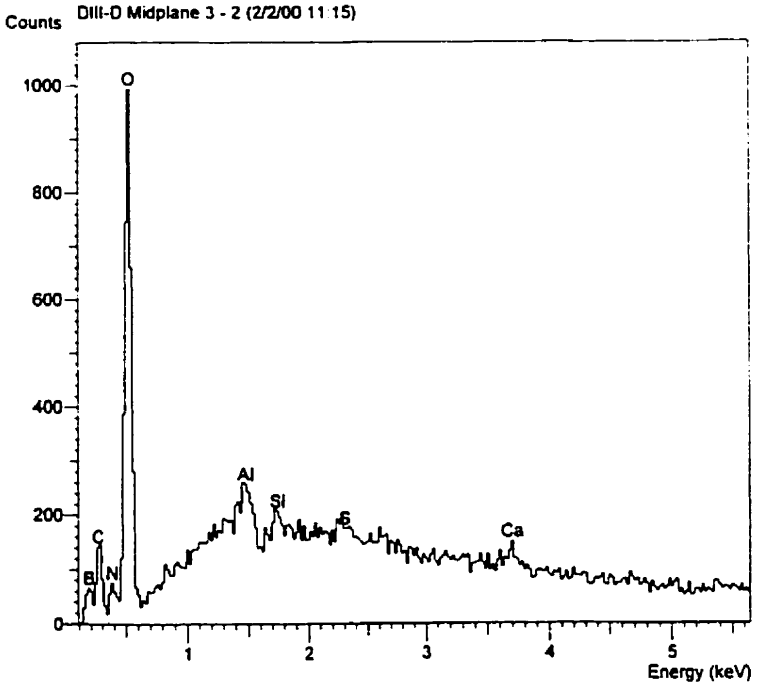

Figure 17: EDX spectrum of sample MP3.

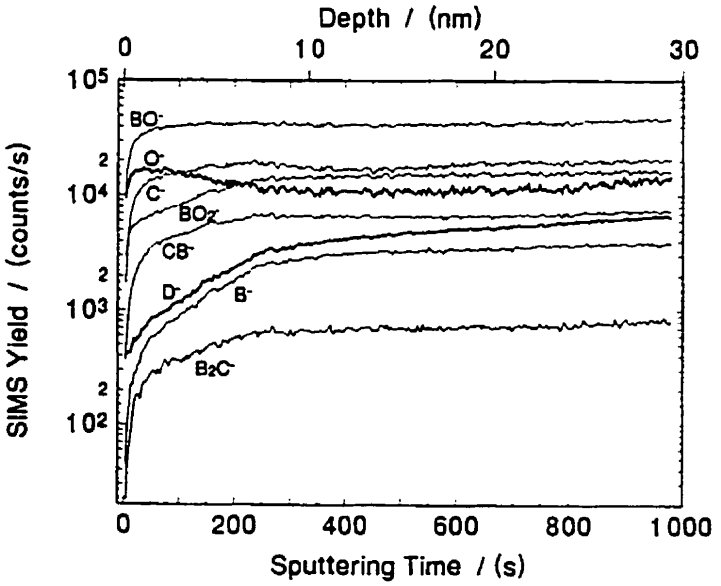

Figure 18: SIMS profile for sample MP3.

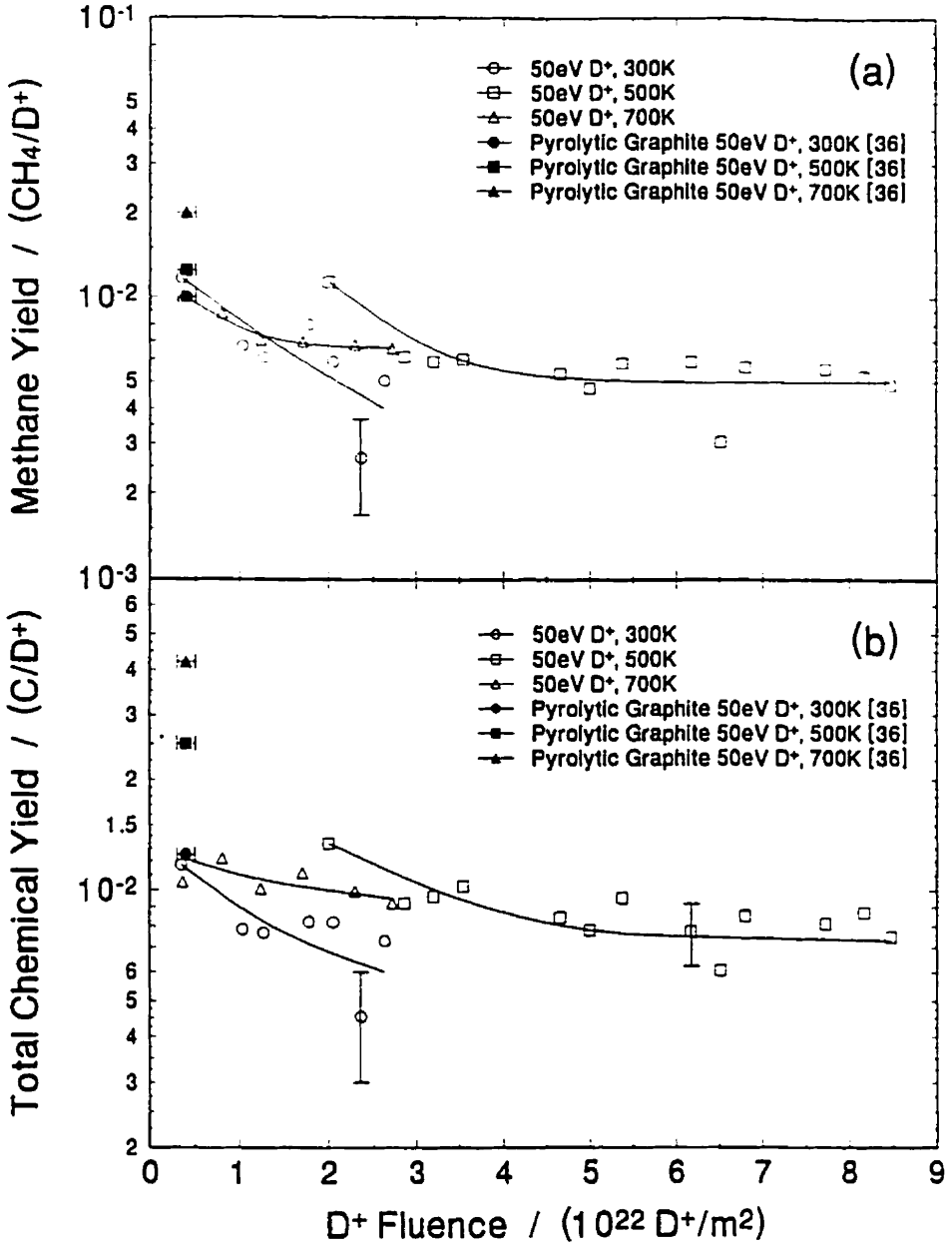

Figure 19: Fluence dependence of 50 eV D^+ erosion measurements: a) C_1D_y and b) $\sum C_xD_y$ on midplane tile sample MP3.

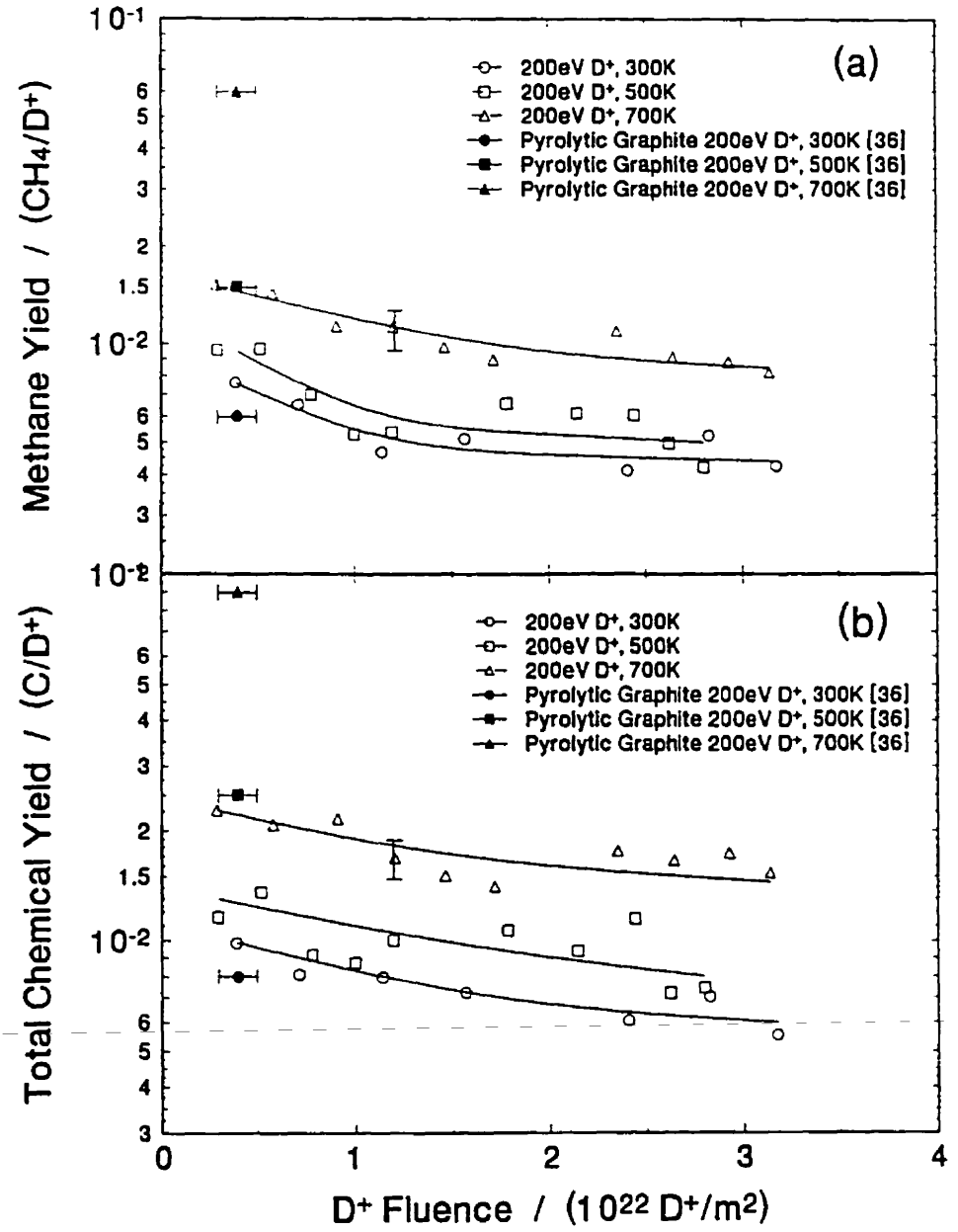

Figure 20: Fluence dependence of 200 eV D^+ erosion measurements: a) CD_4 and b) $\sum C_i D_j$ on midplane tile sample MP3.

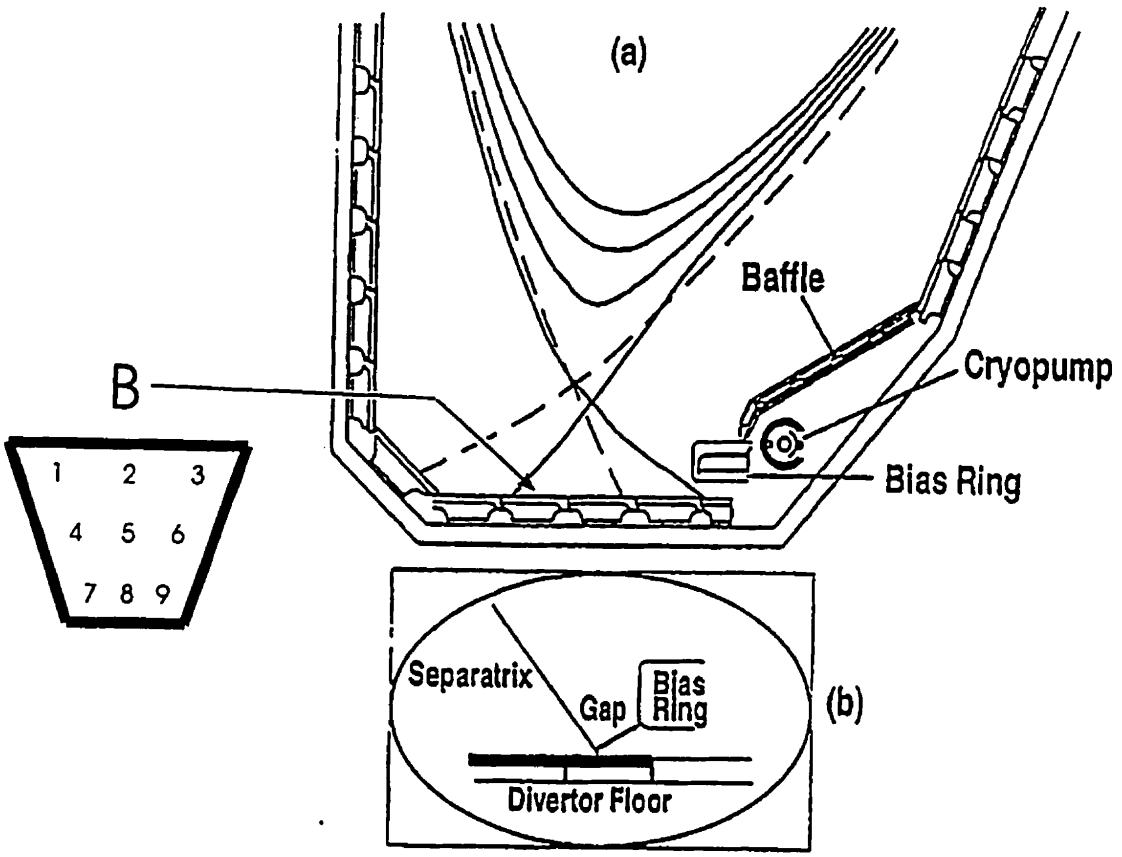

Figure 21: Schematic of the DIII-D divertor region indicating the location of the tile sample B3 [40].

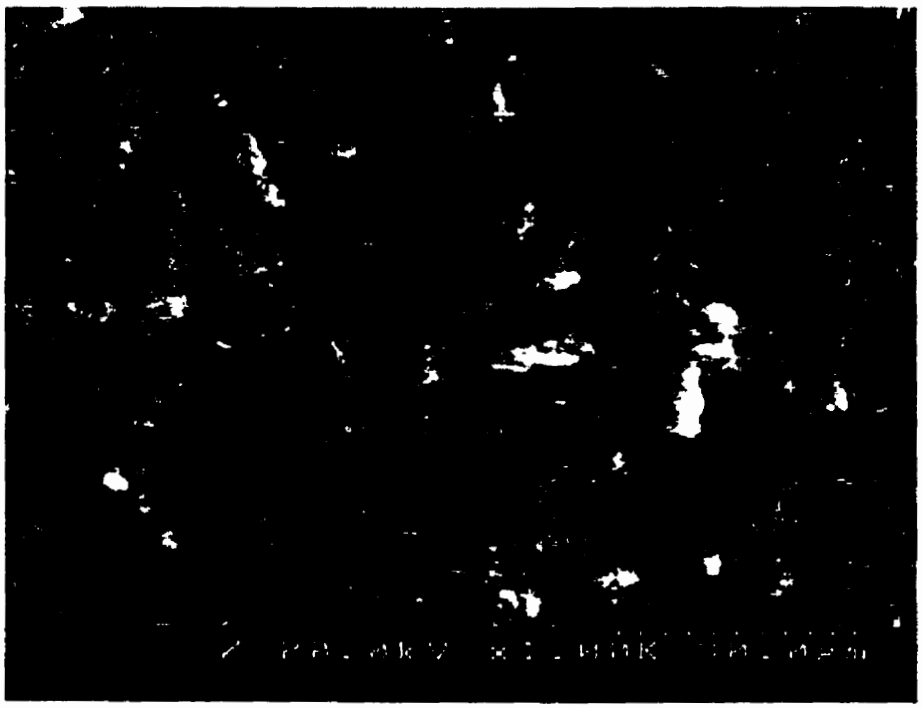

Figure 22: Scanning electron microscopy (SEM) photograph of the surface of sample B3

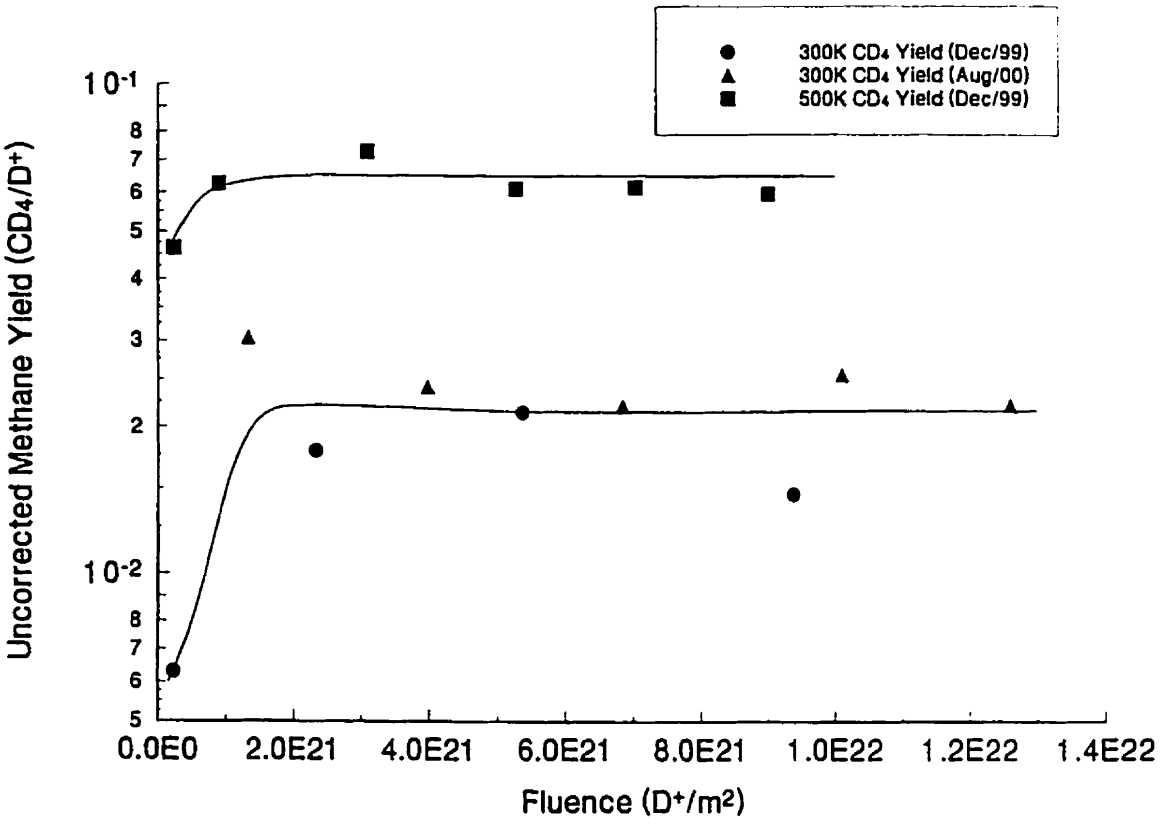

Figure 23: Fluence dependence of 50 eV D^+ CD_4 erosion measurements at 300 K and 500 K for inner divertor tile sample B3.